TAMPERE UNIVERSITY OF TECHNOLOGY

MOHAMMAD MINHAZ AKRAM

THE EFFECT OF SAMPLING IN HISTOGRAMMING AND ANALYTICAL RECONSTRUCTION OF 3D AX-PET DATA

Master of Science Thesis

Examiners: Prof. Ulla Ruotsalainen
M.Sc. Uygar Tuna
Examiners and topic approved in the Computing and Electrical Engineering Faculty Council meeting on 6th of April 2011

ABSTRACT

TAMPERE UNIVERSITY OF TECHNOLOGY
Degree Programme in Information Technology
AKRAM, MOHAMMAD MINHAZ: The effect of sampling in histogramming and analytical reconstruction of 3D AX-PET data.
Master of Science Thesis, 45 pages
January 2012
Major subject: Signal Processing
Examiners: Professor Ulla Ruotsalainen, MSc Uygar Tuna
Keywords: 3D Reprojection, Angular sampling, Axial-PET, Axial sampling, Radial sampling, Sinogram construction, Sinogram correction, Transradial bicubic interpolation.

Improvement in both sensitivity and resolution is achieved by the novel AX-PET concept. This design incorporates axial orientation of long crystal (for coincident detection radially) and orthogonally placed wave length shifter strips (for axial detection). Iterative reconstruction of AX-PET list-mode data was performed by the AX-PET collaboration. But this reconstruction takes long processing time due to large dataset and complexity of algorithm. On the contrary, 3D Reprojection (3DRP) is an analytical image reconstruction technique which can be used to reconstruct the 3D list-mode data of two modules AX-PET demonstrator in shorter time.

In this study, 3DRP method is used for image reconstruction. This process requires histogramming and histogramming requires sampling of the coincident events. Obtaining optimum sampling for better resolution is one of the main goals in the image processing. PET scanner acquires data both in axial and radial direction. Hence, optimum sampling rates for axial, radial and angular directions are required. In this study, histogramming is done with different sampling rates to see their effect in the resolution of the reconstructed images.

The construction of the scanner causes gaps and non-homogeneously sampled Filled of View (FOV). Gap filling method fill the gaps generated from inter crystal and inter module gaps. Coincident detection differs due to difference of the positions of crystals. Normalization is required to have the uniform response from all the detectors. In this study normalization and gap filling were used before 3DRP reconstruction.

Preliminary result shows the ability of resolving the capillary of 1.4 mm. But for the complex phantoms the smallest resolvable inserts was 2 mm. The best results were obtained with the sampling rate of 1mm compared to other sampling rates for different phantoms due to better statistics. The list-mode data of the phantoms used in this study is a low statistics data. To exploit the novelty of AX-PET, high statistics data incorporating more counts is required.

PREFACE

This thesis was carried out in the Methods and Models for Biological Signals and Images (M2oBSI) research group, at the Department of Signal Processing, Tampere University of Technology, Finland.

I would like to express my sincere gratitude to my supervisors Professor Ulla Ruotsalainen and MSc Uygar Tuna who gave me the opportunity to conduct my research. I gratefully thank Professor Ulla Ruotsalainen for organizing partial funding for the work. I am very grateful to my supervisor, Uygar Tuna, for his encouragement, patience and guidance over the time of this exciting thesis work.

I would like to acknowledge all AX-PET collaborators for providing the list-mode data and valuable comments. I am thankful to Kris Thielemans for developing the STIR and keeping it as open source one.

Above all, I am indebted to my family especially to my mother and loving wife.

Tampere, November 2011.

Mohammad Minhaz Akram

CONTENTS

TERMS AND DEFINITIONS

$f(x, y)$	Two Dimensional Image
$g(\theta,s)$	Sinogram
$\delta(x, y)$	Dirac Delta Function
$G(\theta,\omega)$	Two Dimensional Fourier Transform of Sinogram
$F(u, v)$	Two Dimensional Fourier Transform
1D	One Dimensional
2D	Two Dimensional
3D	Three Dimensional
3DRP	Three Dimensional Reprojection
AAA	Advanced Accelerator Applications
AX-PET	Axial Positron Emission Tomography
APD	Avalanche Photodiode
CERN	Conseil Européen pour la Recherche Nucléaire
CoV	Coefficient of Variation
CT	Computerized Tomography
DOI	Depth of Interaction
FOV	Field of View
FPGA	Field Programmable Gate Array
FBP	Filtered Backprojection
FWHM	Full Width Half Maximum
G-APD	Geiger-mode Avalanche Photo diode
GUI	Graphical User Interface
HRRT	High Resolution Research Tomograph
IQ	Image Quality
LDL	Low Discriminator Level
LOR	Line of Response
MPPC	Multi Pixel Photon Counter
LYSO	Cerium-doped Lutetium Yttrium Orthosilicate
NEMA	National Electrical Manufacturers Association
NEC	Noise Equivalent Count
PET	Positron Emission Tomography
PMT	Photomultiplier Tube
PSF	Point Spread Function
PDE	Photon Detection Efficiency

STIR	Software for Tomographic Image Reconstruction
UDL	Upper Discriminator Level
WLS	Wavelength Shifter

1. INTRODUCTION

Positron emission tomography (PET) is an imaging technique mainly used in nuclear medicine. It produces 2D and 3D images of the functional processes in the body. With the advancements in PET technology, PET became popular not only in clinical/human studies but also in pre-clinical/animal studies.

Accurate measurement and visualization of physiological processes is the challenge in modern medical imaging. This challenge can be partially resolved through the improvement of sensitivity and resolution. Sensitivity and spatial resolution are the two key issues in characterizing PET scanner. The resolution is defined as the ability of the scanner to differentiate two closely placed point sources. This resolution is highly dependent on the construction and design of scanner with the effective detection scheme. There are many factors for the degradation of image resolution and the major factors affecting the resolution are attenuation and scattering of the gamma rays, sensor characteristic such as arrangement (spatial distance between detectors) and depth-of-interaction (DOI) encoding in PET detector. Besides, large tracer doses and long data acquisition times contributes to the reconstructed image with high resolution [1]. Moreover, the image reconstruction algorithms including histogramming and data correction have big influence in the quality of the final outcome.

High resolution can be achieved with PET scanner which keeps the DOI information while detecting coincident events. In order to exploit DOI information, the selection of the optimum sampling (radial, axial and angular) and the amount of axial compression in construction of the sinograms from the acquired data plays a significant role. The construction and data acquisition system of the scanner are important parameters for the selection of these different sampling rates.

AX-PET stands for a novel detector design for PET scanners based on axially oriented, elongated crystals and orthogonally placed wavelength shifter (WLS) strips. It aims at significant reduction of the parallax error combined with improved sensitivity and resolution [2]. The full-ring AX-PET scanner setup based on the novel AX-PET concept is still in progress. Only two modules are used to detect the coincident events. Two modules AX-PET demonstrator can detect cross-plane gamma ray events, which are often treated as redundant data. Utilization of redundant data increases signal-to-noise ratio. [3] The quality of reconstructed image is improved with the number of events incorporated into the projections.

The raw data collected by the two modules AX-PET demonstrator are a list of coincidence events and saved as in-house list-mode data. This list-mode data are golden count data and do not consider the effect of random and scatter events. Coincidence events are grouped to create 3D sinogram with the dedicated histogramming process.

Image reconstruction method like analytical or iterative method can be used for 3D reconstruction. Iterative method is time consuming. Recent studies with the two modules AX-PET demonstrator showed that with the dedicated iterative reconstruction method, 1 mm inserts of a NEMA phantom can be resolved [4]. In this study, we are investigating the analytical reconstruction strategies for the list-mode AX-PET data for the first time. This thesis presents the results of 3D Reprojection (3DRP) image reconstruction for the AX-PET list-mode data histogrammed at different sampling rates.

The reconstruction of image from the list-mode data consists of pre-processing steps such as histogramming and dedicated geometrical correction (including estimation of the inter-crystal gaps and inter module gaps. The large dataset containing millions of coincidence event necessitate the compression.

The organization of this thesis is as follows. Chapter 2 deals with an overview of the PET technology mainly focused on the components of typical scanner with their features and limitations. The feature of the AX-PET concept is discussed in chapter 3. Chapter 4 discusses the process of histogramming of the list-mode data to 3D sinogram. Different sampling rates are considered to observe the effect in histogramming. The reconstruction method presented in this chapter is based on analytical approach. Analytical reconstruction methods offer a direct mathematical solution for the formation of an image. Different phantoms such as NEMA-IQ-Mouse-Phantom, Micro-Derenzo, and Mini-Deluxe are used to analyze the functionality of this novel device. Chapter 5 discussed the details of these phantoms. Chapter 6 shows the results of 3DRP reconstruction of histogrammed data for different sampling rates and the effect of sampling through profiles, Full Width Half Maximum (FWHM) calculation and Coefficient of Variation (CoV). Analytical reconstruction results obtained by different sampling for different phantoms are presented in detail. Lastly, the conclusion and discussion presented in chapter 7 highlights the present problems observed in analytic reconstruction and the future research in the reconstruction approach of AX-PET list-mode data.

2. POSITRON EMISSION TOMOGRAPHY

This chapter discusses the fundamentals of positron emission tomography (PET) with the scanner design and data acquisition. Besides, the image reconstruction with data correction scheme is discussed in brief.

PET is a functional imaging modality and widely used in oncology. A solution of radioactive isotope bound to metabolically active molecule is given to the patient. The malignant cells which have the greater metabolism, uptake the solution and radioactive isotopes are deposited to those cells. Emissions of those radioactive particles from these malignant cells are detected by the PET scanner.

In X-ray CT (computerized tomography) the radioactive source is given from outside. PET imaging differs with these contemporary technologies. The radioactive source resides within the subject. The cancerous cells that uptake mostly the radioisotope emits annihilated photons as gamma rays. These gamma rays radiate in every direction. When the scintillation detector pair is in the same line with the two opposite gamma rays, the coincidence is recorded within the specific time window. This is called coincident event and this event is recorded in a single line of response (LOR). The detection is performed from several minutes to hour based on scanner and the type of study. The detected events are recorded in the database for image processing. All the LORs are histogrammed to make projection domain image called sinograms. These 3D sinograms are reconstructed to produce 3D reconstructed image. The entire process of coincidence detection to image reconstruction is shown in the Figure 2.1.

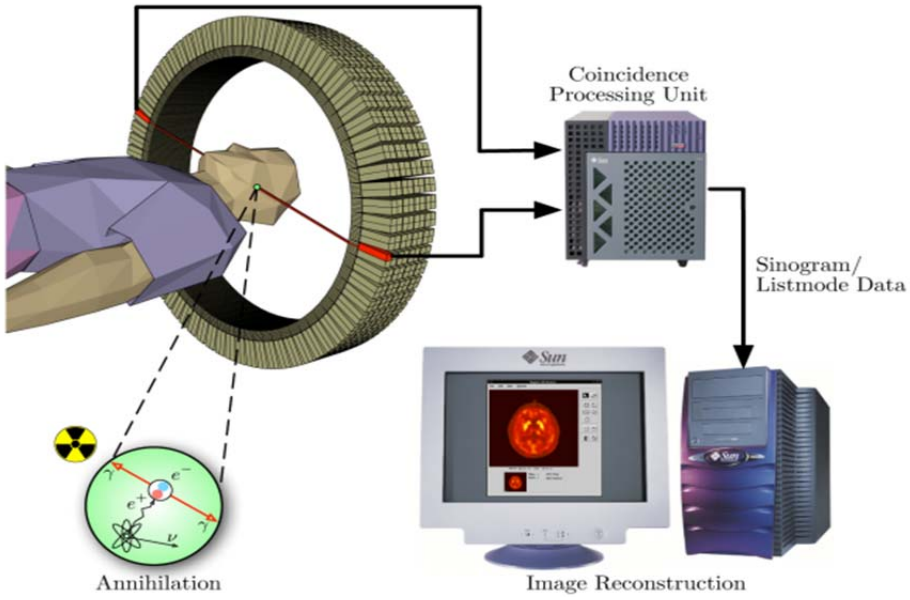

Figure 2.1. *Schema of a typical PET acquisition system [5].*

2.1. PET Scanner

Typical design of a PET scanner is shown in Figure 2.2. PET scanner comprises of multiple rings where individual ring consists of several blocks of detectors. Detector block is the matrix of scintillation crystals coupled with photomultipliers (PMT) or avalanche photodiodes (APD). Data acquisition system based on Field Programmable Gate Array (FPGA) is connected to APD or PMT.

The scintillation crystal converts high-energy photons into visible light. Incident photon in this crystal creates high energy electrons by photoelectric absorption or by Compton scattering. This unstable electron loses its energy and comes back to ground state. This energy is transferred to another electron and becomes excited. Since, it is not a stable one, it decays back to its original state and release the energy as light. This light is received by PMT. PMT amplifies this light and creates electric pulses.

Pulses generated by APD or PMT are passed through processing circuit named as differential discriminator before recording. Lower discriminator level (LDL) and upper discriminator level (UDL) is the two threshold boundaries. If the pulse level is between these levels, the pulse is considered to be true count. Setting the LDL value low increases the sensitivity and more counts can be calculated with the trade of random incidents.

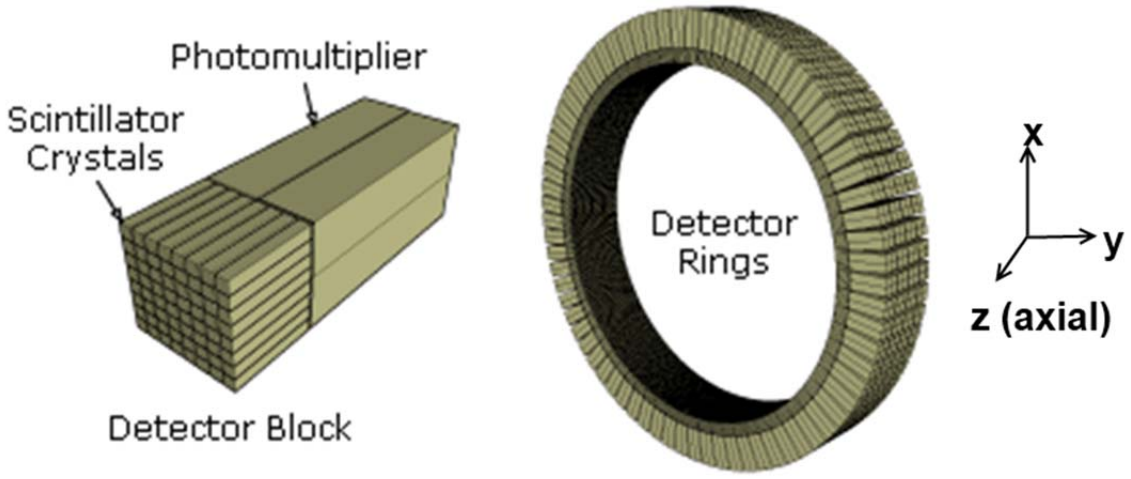

Figure 2.2. *PET-detector system [6].*

The National Electrical Manufacturers Association (NEMA) is the international organization that makes standards for assessing the quality and performance of PET detector systems. It has guidelines for the scanner characterization. Besides it creates the image quality phantoms which are used to test the performance of new PET systems. Major parameters for the assessment of PET devices are spatial resolution, sensitivity, noise equivalent count rate and scatter fraction. Some of them are discussed below.

The spatial resolution of the PET device is defined as the ability to differentiate two consecutive point source placed side by side in the FOV. The less the detected distance of these sources, the better spatial resolution the scanner has.

The detector quality (sensitivity of crystal), placements of detectors and the design of gantry contribute to the spatial resolution. Besides physical phenomena such as light sharing, scatter events and cross-talk also contribute to the spatial resolution.

Another important factor that should be taken into account is the depth at which each photon interacts with the crystal, named as depth of interaction (DOI). Lack of DOI information causes parallax error or radial elongation. This effect is due to the finite distance a photon travels within a crystal before losing all of its energy. Detector ring diameter, detector depth, and the detector material play important role in the determination of correct DOI information. Figure 2.3 shows the effect of parallax error.

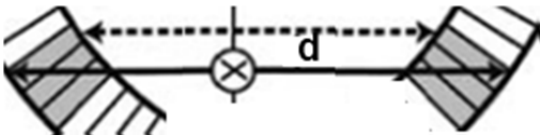

Figure 2.3*. An off-centered event marked as x hit the back of the crystal. The LOR is marked as solid line. But the data acquisition system perceives the LOR as the dashed line. The difference between the original and perceived LOR is marked as* ***d*** *and this incident causes blurring in the reconstructed image [7].*

Reconstructed image quality depends also on the angular and radial sampling. The resolution depends on detector size. Spatial resolution becomes optimum if Nyquist criterion is satisfied. Optimal sampling distance must be less than or at least equal to half of the desired spatial resolution. Sampling distance corresponds to one fourth of the PET detector for the ring PET design [8]. Angular sampling can be done properly if the acquisition is performed over entire range i.e. from 0° to 180°. This interval depends on the data acquisition of individual PET system. Finer angular sampling makes the dataset large and in many cases does not give more useful information.

2.2. Data Acquisition

Simple coincidence detection can be visualized by two detectors placed 180º opposite to each other. The positron-electron ($e^{+}e^{-}$) annihilation in PET creates two 511 keV photons which move opposite to each other. The angle between their trajectories is almost 180º. If the detectors are activated within certain time window and the photons reach the detector pair, then a true coincident event is calculated. This is the ideal case. But, the scanner detects many random events. Besides, objects of different density in the FOV attenuate the photons and within the measured time window the detection is lost. Hence, scanner fails to detect some true coincident events.

Timing window of the logic circuitry and the timing window of the detector must be synchronized to capture the true coincidences. If the pulses are narrow only few coincidences are recorded whereas large pulse window allow many random coincident events.

Single PET detector ring is the primitive design of a scanner and data acquisition is in 2D mode. At present multi layer and multi ring PET scanners are used in PET centers. The rings can be with or without septa. Septa separate one ring from other ring. Figure 2.4 shows the cross section of multi ring PET scanner with and without septa. With septa the data acquisition is considered as 2D whereas 3D acquisition is considered for multi ring PET detectors. In this case coincidences can be recorded between detectors of different rings.

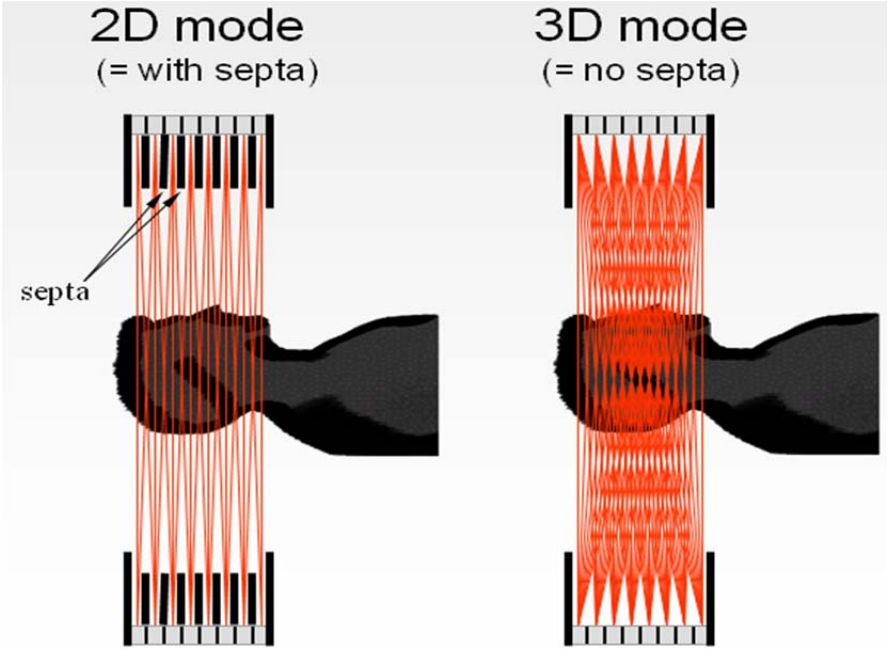

***Figure 2.4**. 2D and 3D PET imaging [9].*

The plane where the detection pair consists of the same ring is called direct plane whereas the detection from neighborhood ring is called oblique plane. The data are organized as the cascade of alternate direct plane and cross plane. If the detector has N number of rings, the number of detection layer is 2N-1. Figure 2.5 illustrates the direct plane and the oblique planes in 3D data acquisition.

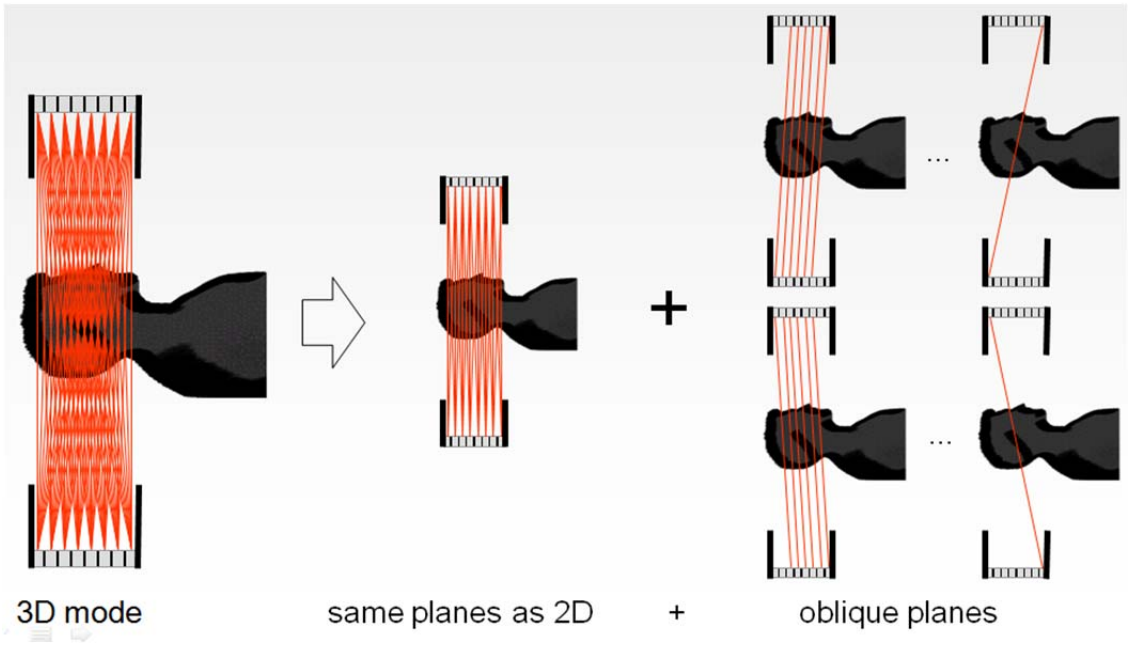

Figure 2.5. *Direct plane and oblique plane acquired from 3D mode PET system [9].*

2.3. Image Reconstruction

PET acquires the data in projection domain. Image reconstruction method applied over these data is required for the proper visualization. The following subsection discusses several concepts related to the analytical image reconstruction methods.

2.3.1. Radon Transform

Figure 2.6 shows the projection $g(s,\theta)$ of the image components over a line at an angle θ which is the line integral of the components of the 2D image $f(x,y)$ resides on that line. The distance between this line and the center of the image is s. The direction of the line with respect to x- axis is θ. This line is called line of response (LOR). Parallel LORs at the certain angle θ create the projection $g(s,\theta)$. The collection of this $g(s,\theta)$ considering all the values of θ over 0^o to 180^o is the Radon transform of the image $f(x,y)$ [10].

The range of s is chosen to cover the selected part of the image specially called field of view (FOV). Radon transform of the image is organized in 2D matrix where the row indicates the value of θ (from 0^o to 180^o to cover entire FOV) and the column denotes radial value (s). This matrix is called sinogram. Figure 2.6 shows the sinogram of the small black circle.

In digital image processing all the values are discrete. Hence, the sampling rate is obvious for discretization. Sinogram consists of angular (θ) and radial values (s). In order to cover entire FOV, the range of θ is from 0^o to 180^o. In general, the increment of 1^o is used. This value is called radial sampling and the choice of this value depends on the structure and data acquisition of different scanners. The range of s is the $\sqrt{2}$ times of the highest value of the dimensions (length and width) of the image. The range is

defined from 0 to s or $-s/2$ to $+s/2$ with the incremental value of Δs. This Δs is called radial sampling.

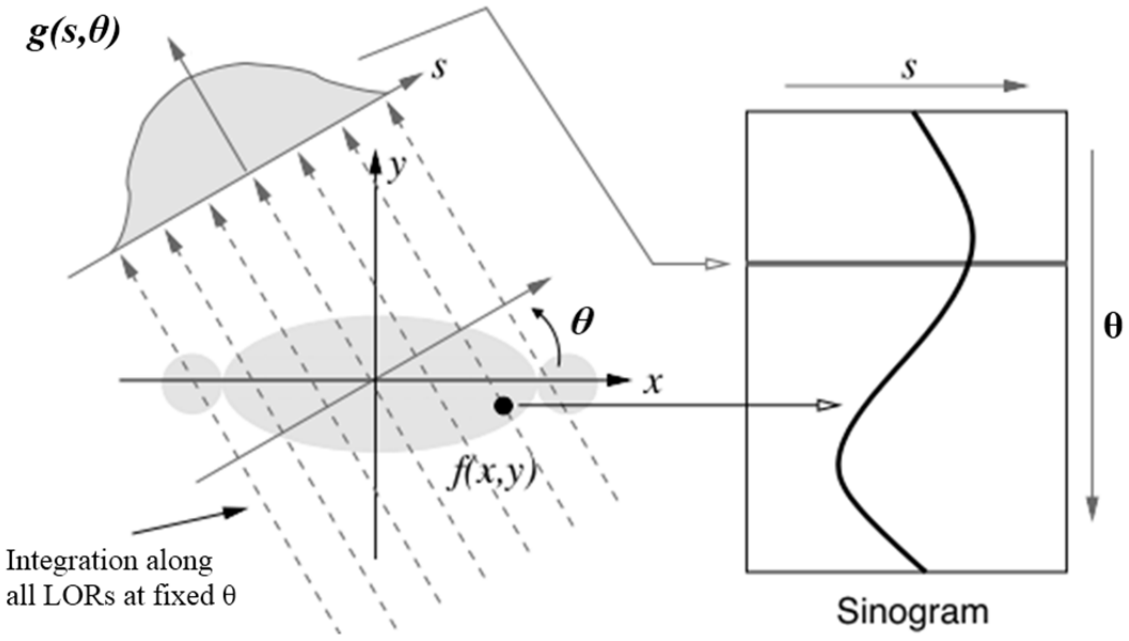

Figure 2.6. *Radon Transform [11].*

The line integration is based on the mapping between cartesian and the polar coordinates. Radon transform based on this line integration follows the Equation (1).

$$s = x\cos\theta + y\sin\theta \tag{1}$$

This Radon transform as described above can be expressed as Equation (2).

$$g(s,\theta) = \int_{-\infty}^{\infty}\int_{-\infty}^{\infty} f(x,y)\delta(s - x\cos\theta - y\sin\theta)dxdy \tag{2}$$

2.3.2. Filtered Backprojection and the Fourier Slice theorem

The Fourier slice theorem tells us that the 1D Fourier transform of the projection function $g(s,\theta)$ equals to the 2D Fourier transform of the image evaluated on the line from which the projection was taken on (the line that $g(s,\theta)$ was calculated from). In this way, all the projections are taken for their respective projection angle and are placed in the 2D frequency domain. To cover the entire 2D plane, infinite amount of projection angles is required. The 2D inverse Fourier transform of this 2D frequency domain image will create the reconstructed image in spatial domain.

Mathematically, the Fourier slice theorem can be elaborated in the following way. The 1D Fourier transform of sinogram $g(s,\theta)$ for projection angle θ is given by:

$$G(\theta,\omega) = \int e^{-j\omega s} g(\theta,s) ds \quad (3)$$

Now, substituting *g(s,θ)* from Equation (2) into the Equation (3)

$$G(\theta,\omega) = \iiint f(x,y) e^{-j\omega s} \delta(x sin\theta - y cos\theta - s) dx dy ds \quad (4)$$

Using sifting property of the Dirac delta function simplifies Equation (4) to

$$G(\theta,\omega) = \iint f(x,y) e^{-j\omega(x sin\theta - y cos\theta)} dx dy \quad (5)$$

The definition of the 2D Fourier transform of 2D spatial function *f(x,y)* is

$$F(u,v) = \iint f(x,y) e^{-j(ux+vy)} dx dy \quad (6)$$

Comparison of Equation (5) and Equation (6) reveals that $u = \omega sin\theta$ and $v = -\omega cos\theta$. This denotes the LOR *g(s,θ)* for projection angle θ. The definition of 2D inverse Fourier transform is as follows

$$f(x,y) = \frac{1}{4\pi^2} \iint F(u,v) e^{j(ux+vy)} du dv \quad (7)$$

Change of variable from rectangular to polar coordinates and replacing $F(u,v)$ with $G(\theta,\omega)$, the ultimate reconstructed image is

$$f(x,y) = \frac{1}{4\pi^2} \iint G(\theta,\omega) e^{j\omega(x sin\theta - y cos\theta)} |\omega| d\omega d\,\theta \quad (8)$$

In order to reconstruct the projections, Filtered Backprojection (FBP) can be used. The idea of FBP is as follows. Individual projection data is transformed to frequency domain and filtered by using any of the filters such as Ram-Lak, Hamming, and Hann. Then the filtered data are inverted back to sinogram domain. This process continues for all projection data in sinogram matrix. Hence, the new sinogram is the filtered version of original sinogram. The output reconstructed image will be created from this sinogram. Output FBP images of a point source for different number of projection are shown in Figure 2.7. Filtering is necessary because Backprojection method incorporates point spread function which blurs the reconstructed image. Filtering gives less priority to low frequency components and enhances components of higher frequency.

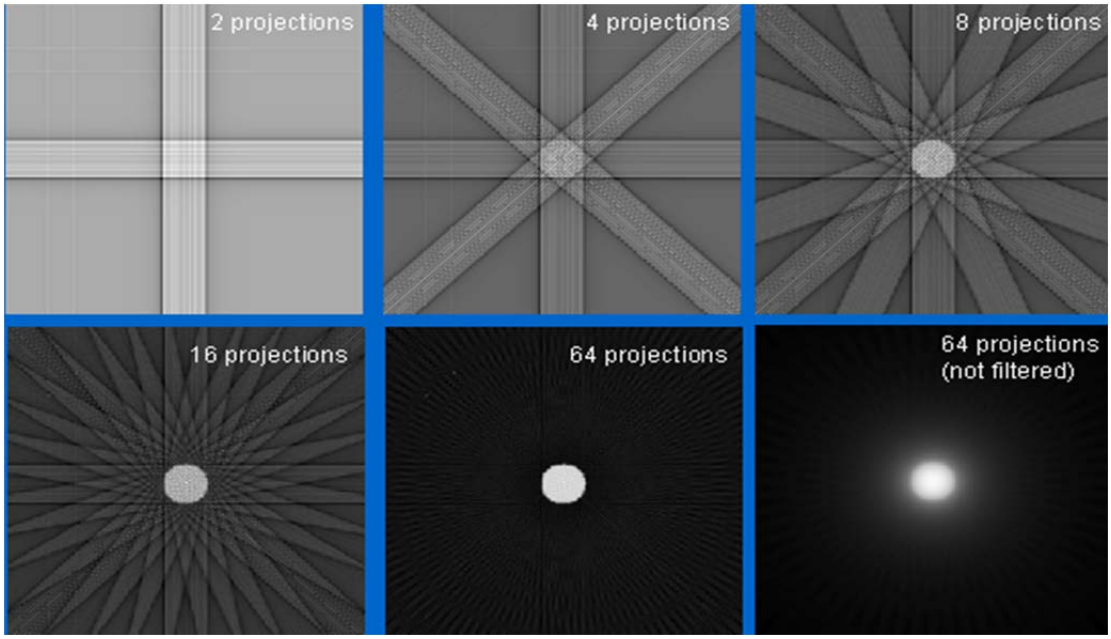

Figure 2.7. *Filtered Backprojection [12].*

Ramp (Ram-Lak) filter is the ideal case for preserving high frequency components. Keeping high frequency components enhance noise and keeping low frequency components blur the image. So, there must be some tradeoff between keeping the amount of high frequency component and the low frequency components. Han, Hamming, Parzen etc are the filters that attenuate both the high and low frequency and keep the mid-band signals. The cut-off frequency can be chosen to control the amount of resolution and noise. Keeping high frequency components enhance resolution and simultaneously increase noise. Figure 2.8 shows the frequency response of different filters used in FBP.

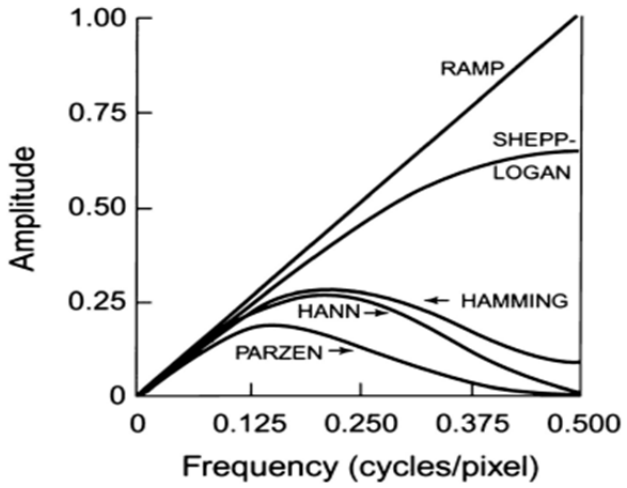

Figure 2.8. *Different filter responses with the cutoff frequency equal to Nyquist frequency [7].*

2.3.3. 3D Reprojection

3D Reprojection (3DRP) is a widely used analytical image reconstruction algorithm for 3D PET. Data acquisition of 3D PET consists of both direct and oblique planes as shown in the Figure 2.5. When the oblique planes are projected to direct plane, unmeasured area is found. This occurs due to finite number of detectors.

Figure 2.9 shows the direct projections and the oblique projections of a scanner with 8 detector pairs. When these oblique planes are projected only central portion of the images can be reconstructed. Other parts of the image cannot be found due to unmeasured LORs. This unmeasured area can be calculated by reprojecting the direct plane to those unmeasured oblique planes. This step is called forward projection which is based on Siddon's algorithm. The forward projecting step estimates all the truncated projection data on fictive rings of the scanner and is equivalent with simulating a PET scanner with a longer axial length.

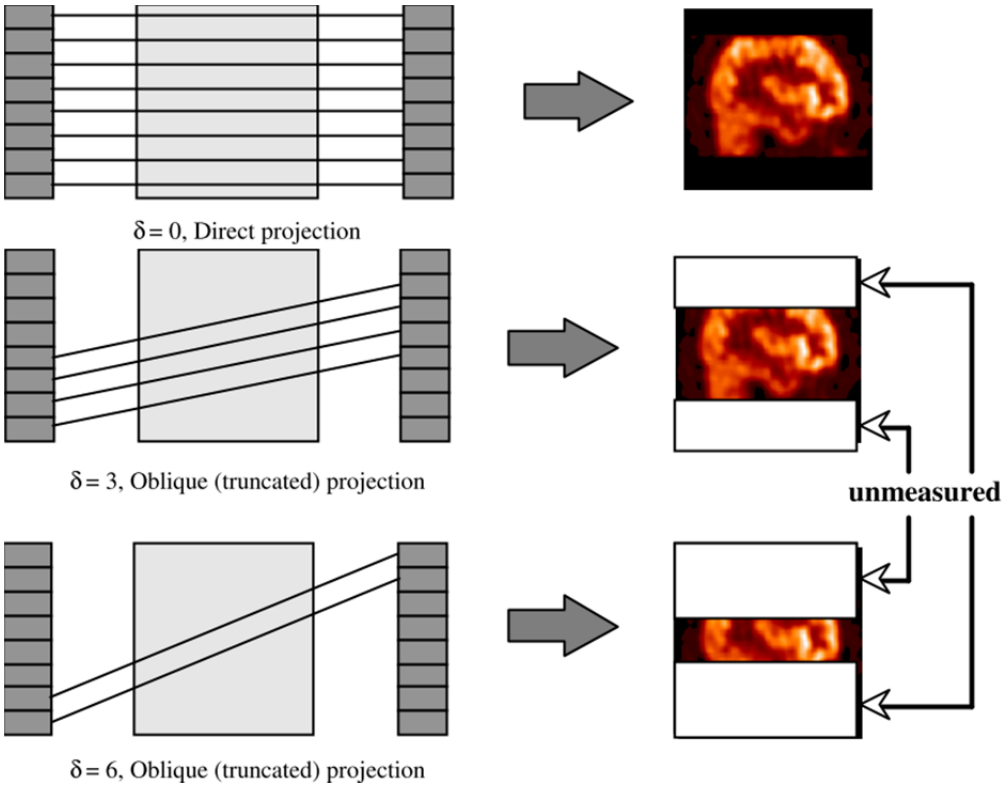

Figure 2.9. *Three different cases show the problem of the projection from oblique plane. Different values of ring difference δ are considered [13].*

At first, 3DRP algorithm reconstructs the direct projections using 2D FBP in order to create first 2D estimate of the image. Afterwards, forward projection of 3D sinogram onto unmeasured parts is performed. 2D estimated data and the forward projected data with oblique projections are projected. The sinograms are filtered using 2D Colsher's filter. Figure 2.10 illustrates the complete process of 3DRP analytical image reconstruction. Design consideration of Colsher filter in 3DRP can be found in [13].

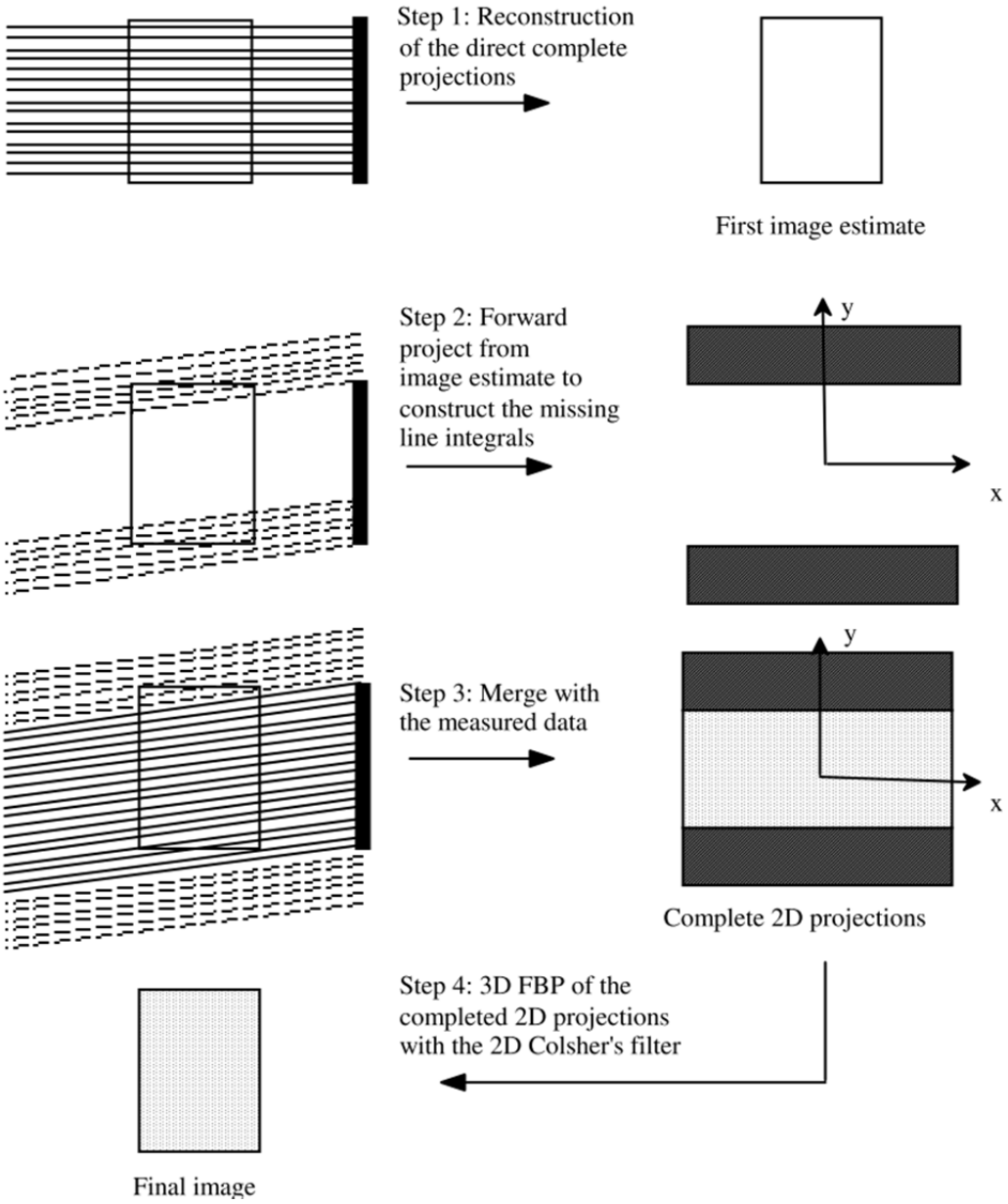

Figure 2.10. *3DRP image reconstruction process [13].*

3. AX-PET

This chapter discusses concept, components of the module and data organization of the novel AX-PET construction. The details of this concept, design and the characteristics of the components are available in [14, 15].

3.1 AX-PET Concept

AX-PET is based on axially oriented Cerium-doped Lutetium Yttrium Orthosilicate (LYSO) crystals and orthogonally placed with wavelength shifter (WLS) strips. Both of them are read out by Geiger-mode Avalanche Photo Diode (G-APD). The unique design of AX-PET allows multiple crystal layers without blurring the DOI information. The right image of the Figure 3.1 shows the axial orientation of long scintillation crystal which is different from the traditional design of PET scanner (shown in the left of Figure 3.1) where the crystals are radially oriented.

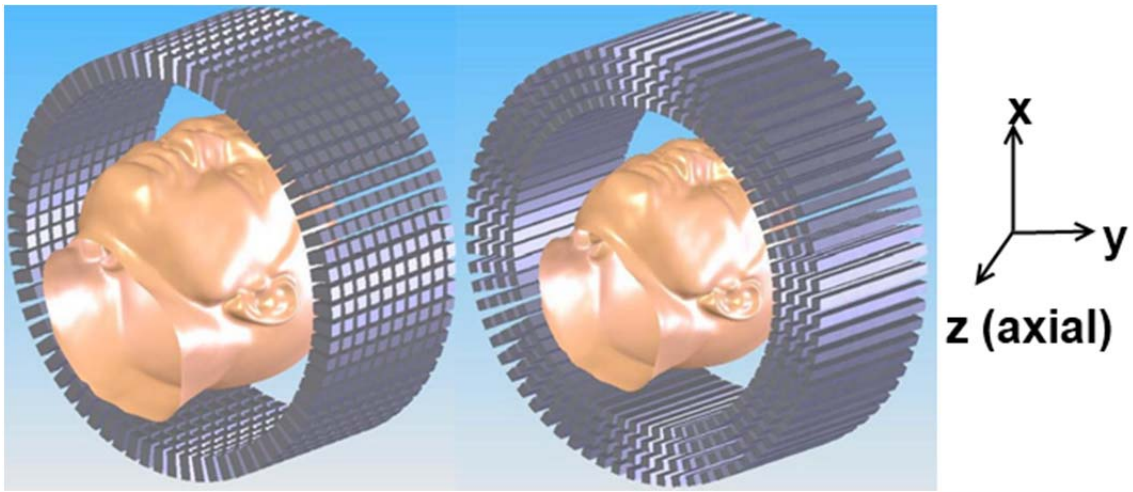

Figure 3.1 *The alignment of the crystals in the AX-PET. The WLS strips are not shown (Left). The conventional PET scanner where the crystals are short and radially oriented (Right). [14]*

Light produced by the gamma interaction with LYSO crystal is readout by G-APD that is named as Multi Pixel Photon Counters (MPPCs). It is placed at the end of crystal bar in one side. The fraction of light escaping from crystal is absorbed by the WLS strip. It changes this light to longer wavelength and is read out by another MPPC connected at one side of WLS strip. The data read out from strips is used to detect the

axial direction (*z* axis) through center of gravity (COG) method. Figure 3.2 shows the gamma interaction detected by both LYSO crystal and WLS strip [14].

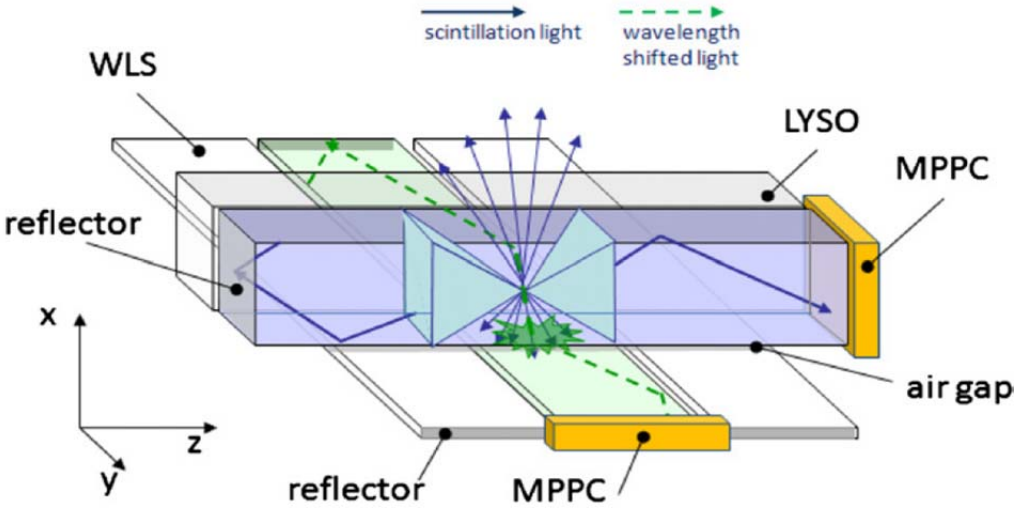

Figure 3.2. *AX-PET gamma detection and z reconstruction principle [15].*

3.2 AX-PET Module

Scanner based on the novel AX-PET concept has not been made yet. Two modules AX-PET demonstrator has been build to test this concept. In the single module of AX-PET demonstrator, the crystals are arranged in 6 layers. Each layer contains 8 crystals. This device provides the gamma interaction point with deposited energy in the transaxial coordinates (*x*, *y*). Since the axial direction (*z* axis) is continuous, the crystals are interleaved by the array of 26 WLS strips to detect the position in axial direction. Figure 3.3 shows the single module of AX-PET detector where the WLS strips are interleaved and orthogonally placed with the crystal arrays.

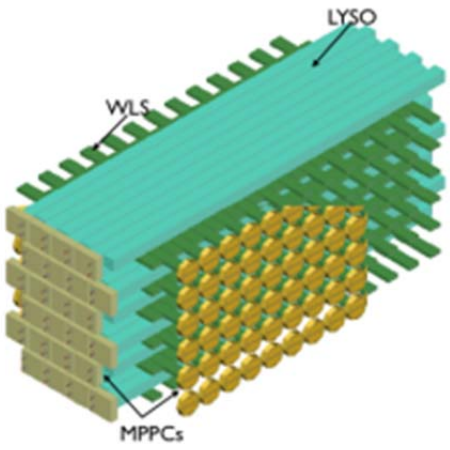

Figure 3.3. *A module of the AX-PET demonstrator with 8×6 LYSO crystals axially oriented and orthogonally interleaved with WLS strips. [15]*

3.3 Data Organization

The novel design of AX-PET scanner allows reconstructing 3D image without parallax error. The resolution of discrete transaxial plane (*x, y*) is limited by the size of crystals and sampling of the data.

Only the golden counts are considered for creating list-mode data. List-mode is the best approach to deal with continuous coordinate while avoiding precision loss in data histogramming. Golden count is the coincident event where only 1 LYSO is fired per module and 1 cluster of WLS strips is associated to hit each crystal. The data from the MPPCs are organized in list-mode format. In the current AX-PET demonstrator, an in-house list-mode data format consists of the detected coordinates of the LORs in the 3D space is used. Figure 3.4 shows the list-mode data organization. Since, one detector pair opposite to each other detects the coincidence, the 3D position is recorded as cartesian (*x, y, z*) coordinate.

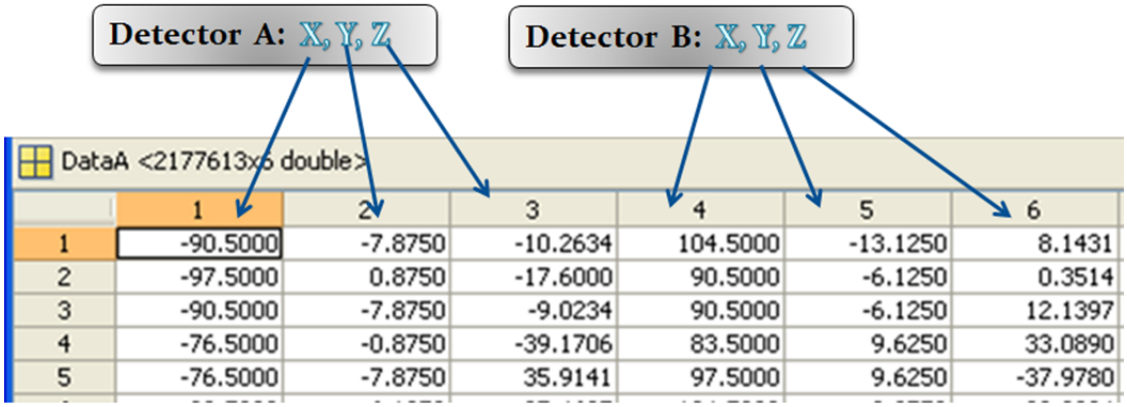

	1	2	3	4	5	6
1	-90.5000	-7.8750	-10.2634	104.5000	-13.1250	8.1431
2	-97.5000	0.8750	-17.6000	90.5000	-6.1250	0.3514
3	-90.5000	-7.8750	-9.0234	90.5000	-6.1250	12.1397
4	-76.5000	-0.8750	-39.1706	83.5000	9.6250	33.0890
5	-76.5000	-7.8750	35.9141	97.5000	9.6250	-37.9780

Figure 3.4. *ListMode data of AX-PET. The values are in millimeters.*

The current design of the AX-PET demonstrator consists of two modules. While one of the modules is fixed, the other module can be rotated by up to ±60°. Therefore, larger and better sampled field-of-view (FOV) is obtained by changing the relative angle between the two modules and by rotating the source. Figure 3.5 illustrates the coverage of two modules in the transaxial plane. It should be noted that one module can be in coincidence with the other module in face-to-face or in an off-the-face configuration (20° in this case). For example, in Figure 3.5, the blue line draws the span of the covered angles by using two-modules by aforementioned configurations and green line illustrates the span of the angles covered as the source is rotated by 20°. Consequently, rotating the source in 18 steps for each of the two module configurations covers all possible angles [23].

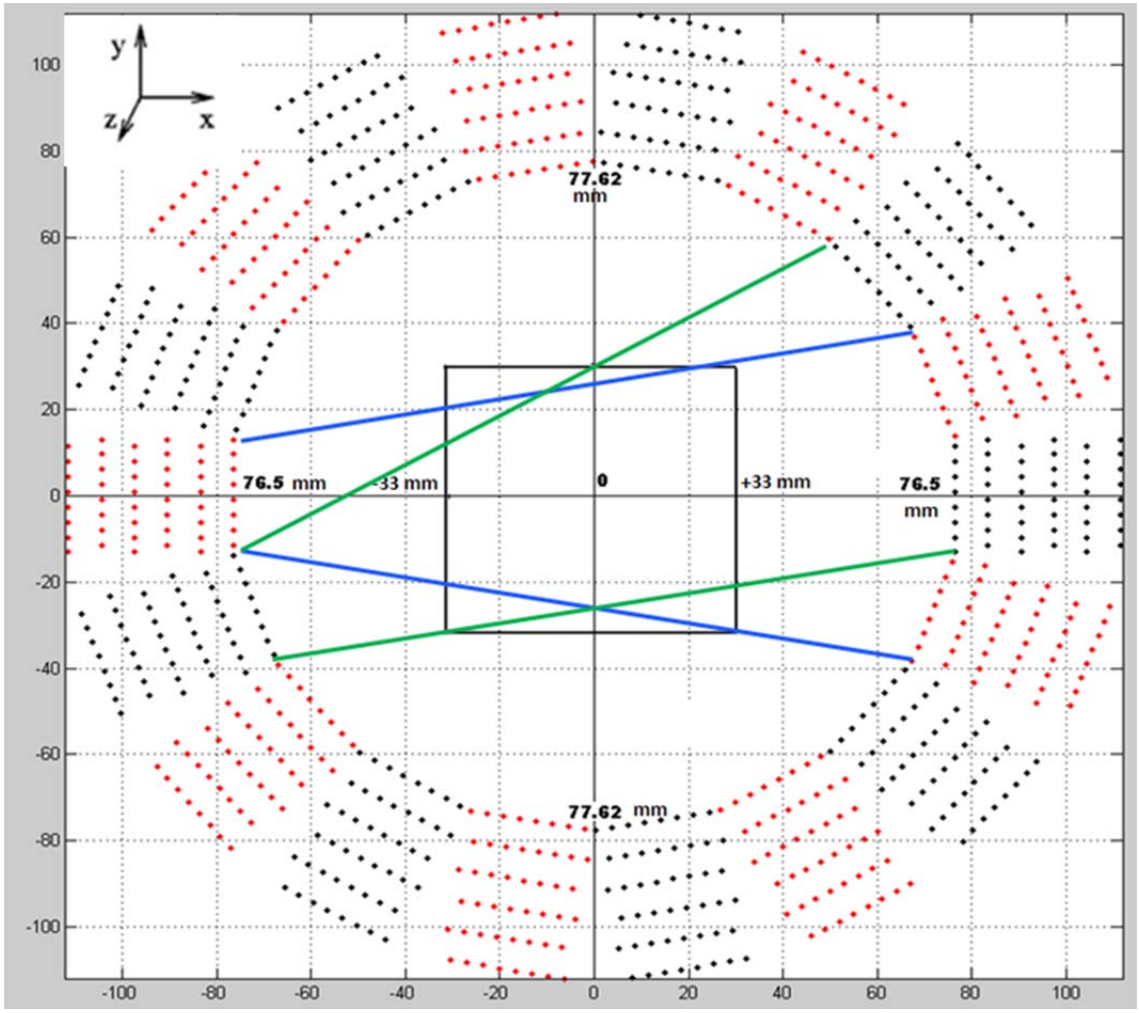

Figure 3.5. *Detectors shown in the transaxial (x-y) plane. LORs can only exist between the detectors in face-to-face or off-the-face (by 20°) configurations. The reconstructed FOV is shown as square (-33 to +33 mm) in the centre. The blue and green lines draw the span of the covered angles when the rotating source is at different positions [23].*

4. HISTOGRAMMING AND ANALYTICAL IMAGE RECONSTRUCTION

The chapter discusses the approach for analytical image reconstruction for the AX-PET list-mode data. It starts from the projection of list-mode data and ends with the image reconstruction process.

Histogramming of acquired data, creation of sensitivity matrix, gap-filling with transradial bicubic interpolation method and 3DRP are the intermediate steps for the ultimate image reconstruction. The entire steps followed to reconstruct the image are schematized in Figure 4.1.

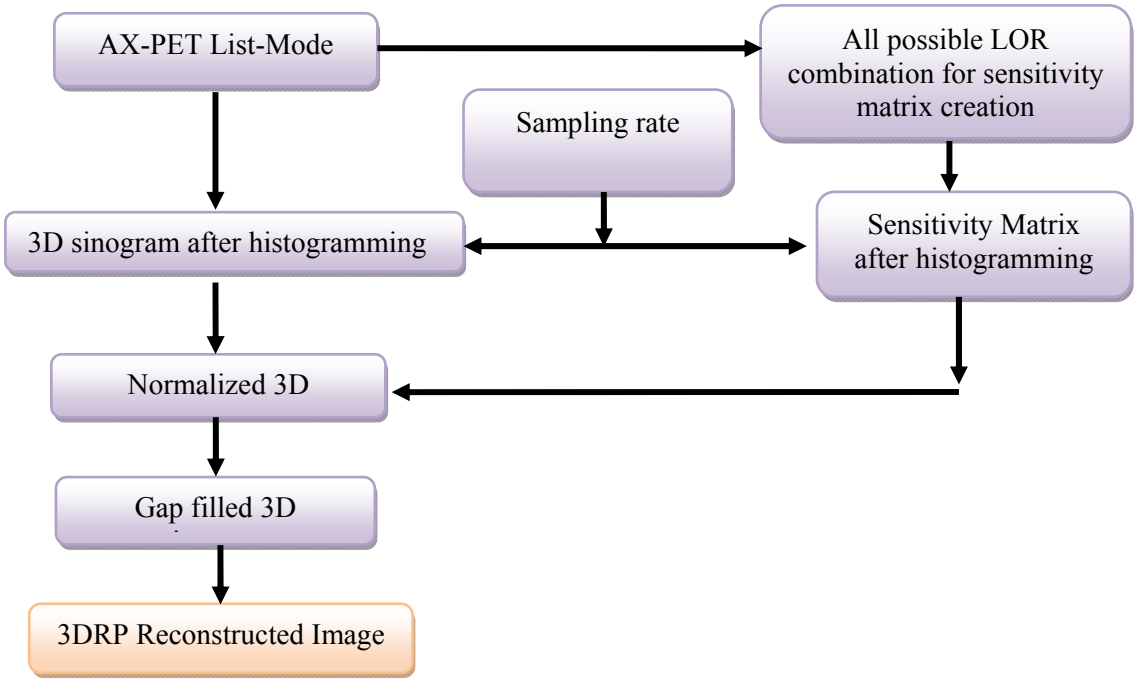

Figure 4.1. *Complete process of histogramming and 3DRP reconstruction of list-mode AX-PET data.*

4.1. Histogramming

The 3D list-mode data were histogrammed by using span9 axial compression scheme. A FOV of 67 x 67 x 80 mm^3 was considered for the image reconstruction. Before histogramming, the 3D coincidence points were projected to inner ring perimeter which became new positions of detection. Figure 4.2 shows the projection in 3D space. The discrete transaxial coordinates (*x, y*) were used directly in the histogramming. However,

the continuous axial coordinates (z) were discretized according to the radial sampling used in the construction of the sinograms.

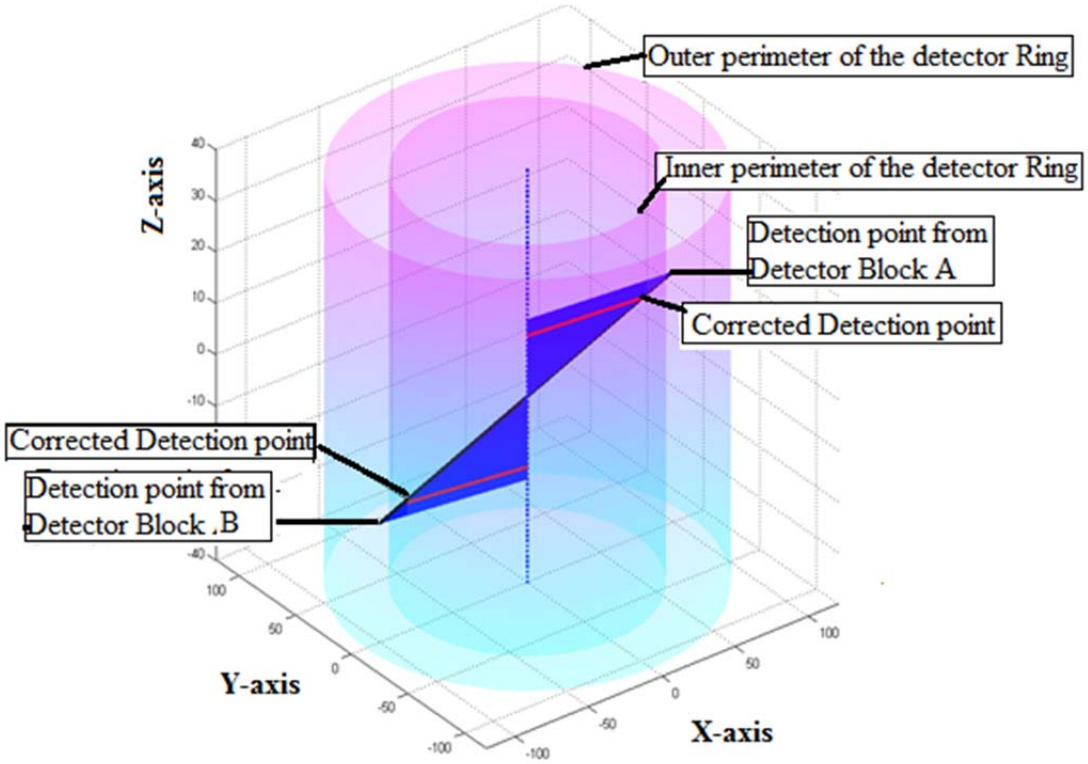

Figure 4.2 *Projection of detector point to inner detector ring for a single detected event.*

The pitch of the crystals in y direction (3.5 mm) was considered in the choice of the radial sampling. Hence, the radial sampling rate of 0.875 mm is chosen. This value is one fourth of the crystal pitch. This choice is based on [8]. Since, the data from multi layers are projected to inner ring, the positions of the coincident events are more even in the middle of sampling steps of 0.875 mm. This projection gives the opportunity of higher sampling rate. Hence, 0.4375 mm which is half of the previous sampling rate was also chosen. Besides, 1mm radial sampling rate was considered to have the similarity of the previously reconstructed image of the AX-PET collaboration. Axial direction in the AX-PET concept is continuous. For the simplicity, the axial sampling rates are twice of the radial sampling rates. For the angular sampling, we used 1° increments which yielded 180 angular views in the constructed sinograms. Figure 4.3 illustrates the crystal pitch in transaxial view of the scanner [23].

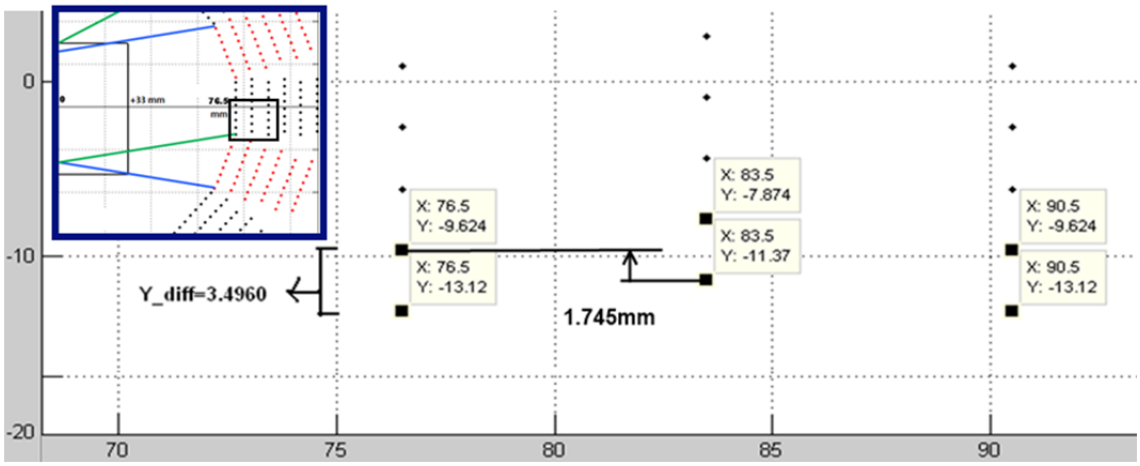

Figure 4.3. *Distance of consecutive detection point according to crystal pitch in Y-axis. The value in the X-axis and Y-axis corresponds to detected position in transaxial view of AX-PET scanner as shown in the inset figure.*

Even though the list-mode data had only golden events and it is not required to apply correction for random or scattered events, we had to apply geometrical corrections to the histogrammed data and data estimation methods for the inter-crystal gaps [17]. For the geometrical correction, we calculated all possible LORs which can be recorded by the current rotating two-module AX-PET demonstrator. The obtained sensitivity map which shows the probabilities of the individual detector pairs in recording the events was used to correct the constructed sinograms. Depending on the used radial sampling, the inter-crystal gaps in the sinogram change in shape and magnitude [23]. Figure 4.4 illustrates the sensitivity map for the sinogram belonging to the transaxial segment. The missing parts of the data were estimated by using the transradial bicubic gap-filling method published previously in [18, 22].

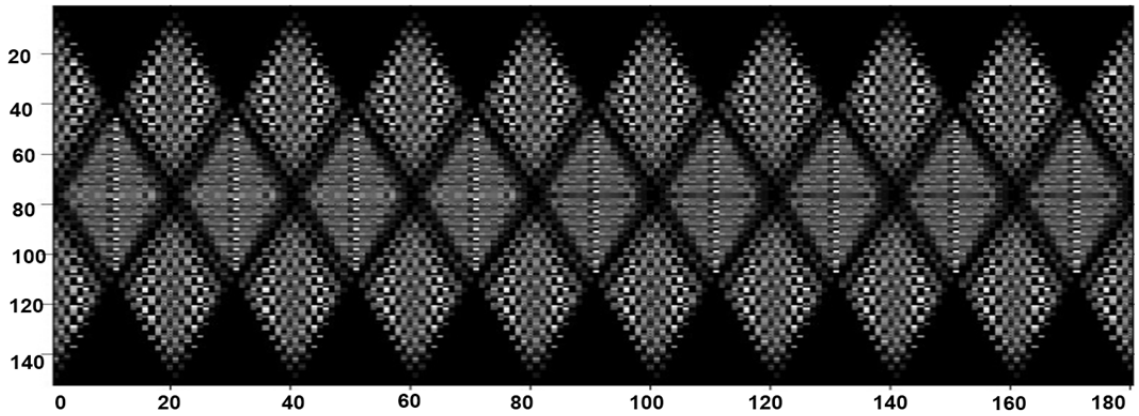

Figure 4.4. *Sensitivity map obtained by using the radial sampling of 0.4375 mm and angular sampling of 1°. While the white sinogram bins are the most sensitive parts, the black sinogram bins cannot register event due to the inter-crystal gaps and geometry of the rotating AX-PET gantry [23].*

For span9 axial compression scheme, the obtained 3D sinogram data were of size 153 x 180 x 7077 (radial samples x angular views x slices) organized in 39 segments for the radial sampling of 0.4375 mm, 77 x 180 x 1737 in 19 segments for the radial sampling of 0.8750 mm and 67 x 180 x 1401 in 17 segments for the radial sampling of 1 mm.

4.2. Analytical image reconstruction

The corrected 3D sinograms were reconstructed analytically by using 3DRP method with Colsher's filter. The implementation uses FBP (filtered back projection) on 2D data to generate image to be used for reprojection. In this case, ramp filter was used for 2D FBP. Alpha parameter for ramp filter was 1 whereas cut-off for ramp filter (in cycles/pixel) was 0.5. Alpha is an arbitrary positive real number that determines the shape of the window. As an example, the value of zero for alpha parameter make rectangular window. Window function is necessary before doing filtering in Fourier domain. Stretch factor for Colsher's filter in axial and radial direction of 2 were used. This factor defines the amount of sub-sampling for Colsher on finer grid. The higher the number is, the better the filtering is with the cost of longer reconstruction time. Alpha parameter for Colsher's filter in axial and radial direction was 1. Normalized cut-off frequency for Colsher's filter in axial and radial direction (in cycles/pixel) was 0.5. The final reconstructed images were of size 153 x 153 x 351 for the radial sampling of 0.4375 mm, 77 x 77 x 171 for the radial sampling of 0.8750 mm and 67 x 67 x 153 for the radial sampling of 1 mm.

5. MEASURED PHYSICAL PHANTOMS AND EVALUATION METHOD

This chapter presents the dataset and the evaluation techniques used in the work. The performance of the aforementioned histogramming and 3DRP reconstruction with gap filling were assessed with the list-mode dataset of different phantoms.

5.1. Numerical Phantom

Cross-sectional diagram of NEMA NU 4 image-quality phantom having 5 inserts is taken as numerical phantom. Figure 5.3 shows the phantom from which this numerical phantom was generated. The image is processed in MATLAB and only the inserts are filled with white color. The backgrounds are colored as black. The white colored inserts signify the filled form of radioactivity. This numerical phantom is used to observe the effect of gap-filling and normalization. Figure 6.2 shows this numerical phantom and its reconstructed image.

5.2. Measured Physical Phantoms

Medical imaging methods and devices are commonly evaluated through computer simulations. Phantoms are used to model patient anatomy and physiology. Thus it contributes to the evaluation of medical imaging devices and techniques. To measure the performance of AX-PET concept, different phantoms are used. Performance of two modules AX-PET demonstrator was measured with capillary, micro-Derenzo, Mini Deluxe and other phantoms made at CERN. The demonstrator was fully assembled, set in coincidence and used to acquire data from different sources. These sources are described in the subsections below. All of the phantoms are filled with [18F]-FDG (FDG) in water. Details of the data acquisition are available in [19].

Point sources are very useful to measure sensitivity and spatial resolutions. But they are not sufficient to discover artifacts due to having a non complex structure. To test the sampling effect on resolution, complex phantoms such as Derenzo, Mini-Deluxe were used.

5.2.1 Capillary Phantom

To study the influence of parallax error on the resolution, the source was scanned at various radial distances. Capillary phantom is one of the good examples of this kind of

study. The data dealt in this section refer to a set of acquisitions of 8 thin capillaries placed in the transaxial plane and separated by 5 mm pitch in transaxial (y) coordinate. The length of each capillary is 30 mm while the diameter is 1.4 mm. Figure 5.1 illustrates this phantom.

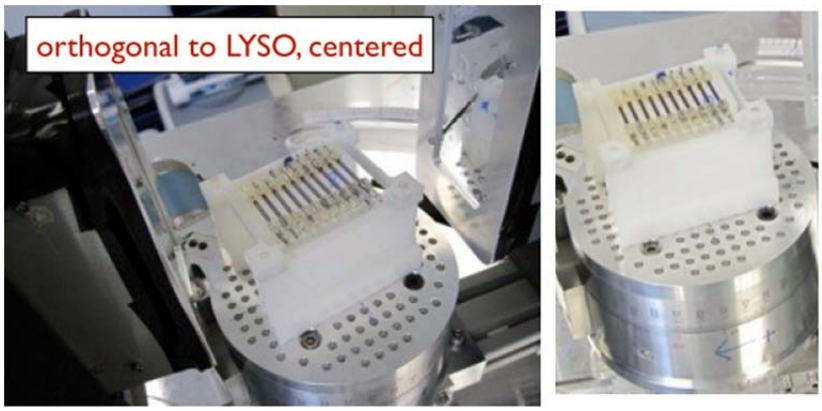

Figure 5.1 *Phantom consist of 8 thin capillaries* [19]

5.2.2 Mini Deluxe phantom

Mini Deluxe Phantom custom made at CERN is the largest phantom with full FOV coverage for AX-PET measurement. This phantom is mainly used for small animal system evaluation especially spatial resolution [20].

This phantom has six regions where each region has several rods of uniform diameters. Rod diameters are 1.2, 1.6, 2.4, 3.2, 4.0 and 4.8 mm. Height of rods are 34 mm. Entire phantom is housed in a cylinder with outside diameter of 83 mm and inside diameter of 76 mm. All images in Figure 5.2 are shown from the transaxial view. Detail of this phantom is available in [19].

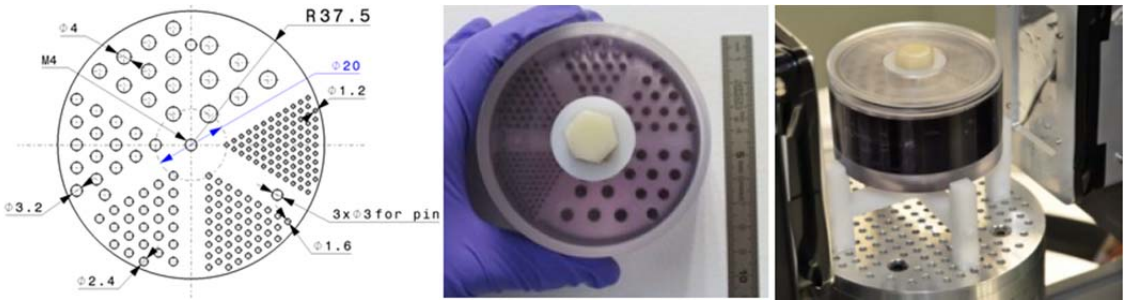

Figure 5.2. *MiniDeluxe Phantom* [19]

5.2.3 NEMA-IQ-Mouse-Phantom

The NEMA NU 4-2008 image-quality phantom commercially named as NEMA-IQ-Mouse-Phantom is a 50-mm-long; 30-mm-diameter cylinder consists of different

regions to analyze different aspects of image quality. A schematic view of the phantom is shown in Figure 5.3.

The first 20 mm of the phantom body are solid, with 5 fillable rods with diameters of 1, 2, 3, 4, and 5 mm. A fillable cylindrical chamber with 2 hollow cylinders (length, 14 mm; inner diameter, 8 mm) makes up the remaining 30 mm of the phantom. Both cylinders are filled with nonradioactive cold water in the measurements campaign at Advanced Accelerator Applications (AAA) held on July 2010. In this thesis, this phantom is named as NEMA-IQ-Mouse-Phantom A. The reconstructed images of this uniform nonradioactive region may still display activity as a result of scattered photons, nonzero positron range, random, or other effects. On 2011 campaign, one of these cylinders is filled with air, and the other with nonradioactive water. The 5 rods and the large chamber, excluding the cold cylinders, were filled with radioactive solutions. In this thesis, this phantom is named as NEMA-IQ-Mouse-Phantom B. The details of this phantom are available in [19].

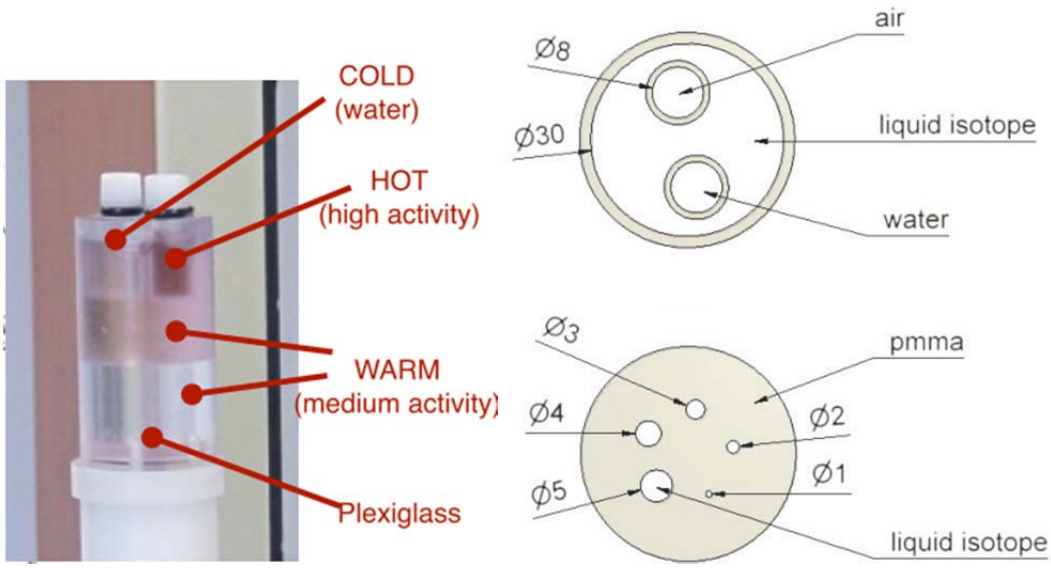

Figure 5.3. *Cross-sectional diagram of NEMA NU 4 image-quality phantom. In the above images, gray colored regions represent solid polymethylmethacrylate, and white regions represent hollow, fillable compartments (Right). The different region of phantom made at CERN(Left) [19].*

5.2.4 Micro Derenzo phantoms

Micro Derenzo phantom A consists of 14 inserts and the diameter of the cylinders of three categories are 1.5, 2 and 2.5 mm. Figure 5.4 illustrates the regions.

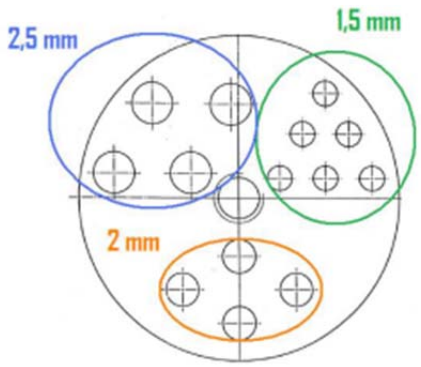

Figure 5.4. *Micro Derenzo phantom A [19].*

The Micro Derenzo phantom B as shown in the Figure 5.5 has the inserts of 5 different sizes. Inserts marked as 'A' have the diameter of 1.3 mm. The entire phantom has the diameter of 15 mm and the height is 19.5 mm. The others are 'B' (1 mm), 'C' (1.7 mm), 'D' (2 mm) and 'E' (0.8 mm).

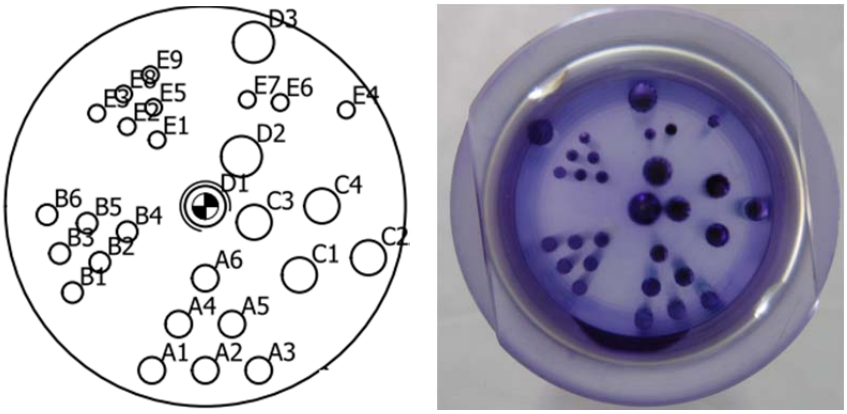

Figure 5.5. *Transaxial view of Micro Derenzo phantom B [19].*

5.2.5 Uniform phantom

This uniform phantom named as D60H70 has the volume is 194 cm^3. It is used to measure the uniformity and noise characteristic. Besides it is used for normalization and quantitative calibration. Figure 5.6 shows the hollow cylinder filled with radioactive water and placed in the rotating table.

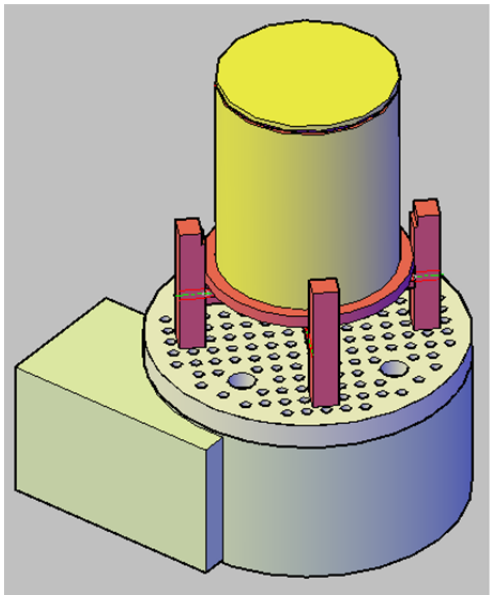

Figure 5.6.*Uniform phantom [19].*

The number of golden events (the LORs in the list-mode data) for different phantoms is shown in the Table 5.1.

Table 5.1. *Number of counts of the phantoms reconstructed in the thesis.*

Phantoms	Number of Counts
Capillary	17.5M
NEMA-IQ-Mouse-Phantom A	21.3M
NEMA-IQ-Mouse-Phantom B	30.7M
Mini Deluxe phantom	27.3M
Uniform phantom	28.5M
Micro Derenzo phantom B	40.5M
Micro Derenzo phantom A	20.1M

5.3. Evaluation Method

In order to evaluate the imaging performance and to compare image quality of AX-PET for different sampling, Full Width Half Maximum (FWHM) values were measured. FWHM is the width measured at half level between the continuum and the peak of the line. The resulting images of the phantoms are reported in the result section.

5.3.1. Resolution Measurement

The reconstructed images were investigated to study the resolution. Resolution is the ability to separate closely spaced objects. These images are compared to determine the relationship between sampling and image resolution. Parameters for assessing sampling effect on spatial resolution of these images can be extracted by the measurement of the

profiles. The measurement of the profile gives access to the number of the counts per pixel of the selected part of image. Line profile such as: the width of the line, the line FWHM, the peak intensity can be used.

In this study, we want to compare different sampling for the same list-mode data with the goal of determining which has the best spatial resolution. In other words, we want to know which sampling can detect the smallest object.

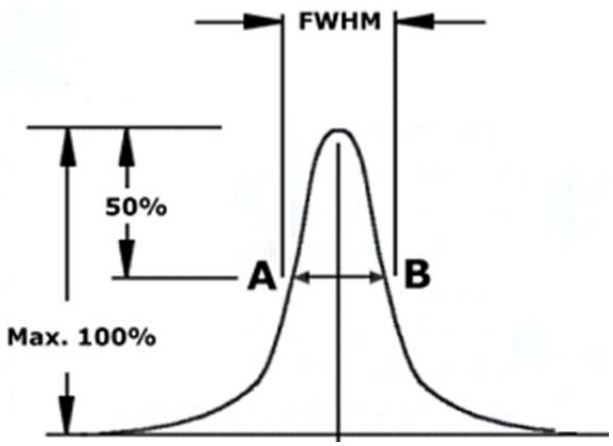

Figure 5.7. *FWHM of the ideal Gaussian curve [24].*

Figure 5.7 shows the FWHM calculation from the original Gaussian distributed curve. The curve is expressed as power signal. When the information does not belong to power or energy, then FWHM is calculated at 70.7% (instead of 50%) of the peak value. In the real data, the distribution may not be Gaussian. Then it requires some curve fitting method to make a Gaussian distribution based on original data. Figure 5.8 shows the Gaussian curve fitted data over original discrete data.

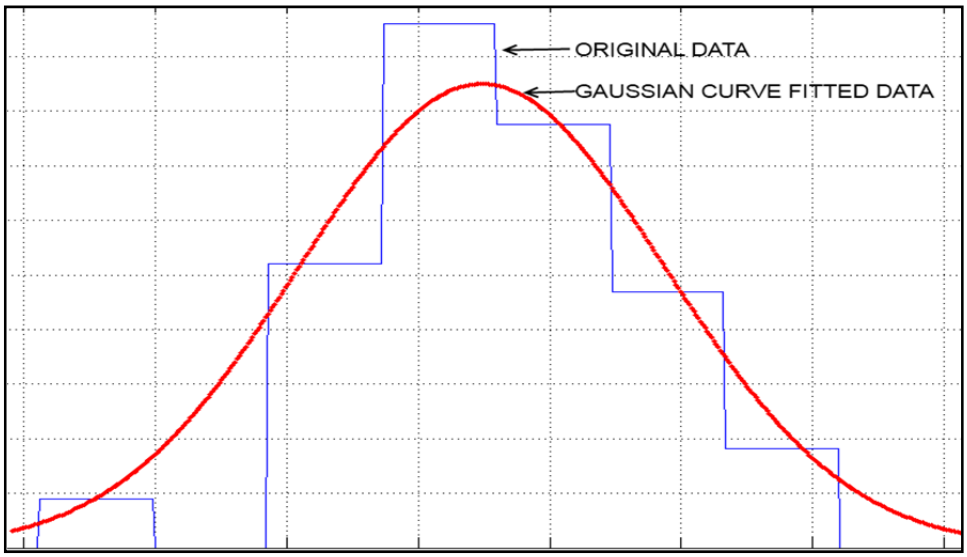

Figure 5.8. *Gaussian curve fitted data over the original discrete data. Bicubic interpolation is used for curve fitting.*

5.3.2. Uniformity Measurement

Uniformity is a measurement of the deviation of the pixels of the homogeneous region of the reconstructed tomographic image with respect to the mean value. The reconstructed images are analyzed by determining the number of counts in any region of interest (ROI) inscribed within a rectangle in the image of the phantom [21]. Coefficient of Variation (CoV) is such a measurement that can estimate the uniformity in the ROI. It is the standard deviation normalized by mean. For the perfectly uniform image the CoV is zero. It is a dimensionless number. CoV calculation is defined as Equation (9).

$$CoV(f(x,y)) = \frac{\sqrt{\frac{1}{MN}\sum_{x=1}^{M}\sum_{y=1}^{N}\left[f(x,y)-\frac{1}{MN}\sum_{a=1}^{M}\sum_{b=1}^{N}f(a,b)\right]^2}}{\frac{1}{MN}\sum_{x=1}^{M}\sum_{y=1}^{N}f(x,y)} \times 100 \quad (9)$$

f(x, y) and *f(a, b)* is the ROI of the reconstructed image. *M* and *N* are the dimensions of selected ROI [22]. The denominator in the equation is the mean value of ROI.

6. RESULT

This chapter shows the 3DRP reconstructed images of AX-PET list mode data. Images of capillary, NEMA-IQ-Mouse-Phantom, Micro-Derenzo, Mini-deluxe and uniform phantoms were reconstructed. Results show the effect of different sampling used in histogramming.

6.1 Effect of Gap filling and Normalization

The transaxial view of 5 inserts of numerical NEMA-IQ-Mouse-Phantom was taken from [19]. From this phantom sinogram was generated by using MATLAB's imradon function. That sinogram was multiplied with sensitivity matrix to have the inter-crystal gap artifacts. From the Figure 6.1, it is observable that AX-PET data suffers from low statistics. Besides it incorporates a lot of scattering events. Inter-crystal gap and inter module gaps are a regular patterns over the sinogram. Those can be resolved using different methods described in [18, 22].

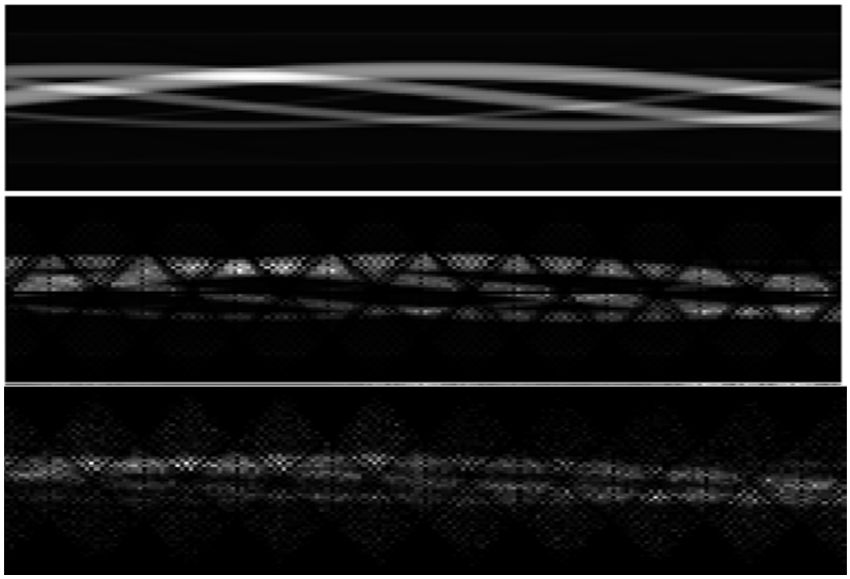

Figure 6.1. *Above Figure shows the sinogram of original NEMA-IQ-Mouse-Phantom. Middle figure is the sinogram multiplied with sensitivity matrix to have the inter-crystal gaps. Figure at below shows the sinogram generated from histogramming of AX-PET list mode data. Resolution of 1mm was considered. X axis shows the angular views from 1° to 180° whereas Y axis shows the radial distance from -33 to +33 mm.*

Figure 6.2 shows the reconstructed images of the phantom generated from the sinogram shown in the Figure 6.1. Normalization and gap filling (Inpainting method) were applied individually to observe the effect in the reconstructed images. The sampling of 1 mm was considered. Figure 6.2 (d) shows that reconstruction after normalization and gap filling is the best approach. Figure 6.2 (b) and (c) shows the effect of only gap-filling and normalization individually.

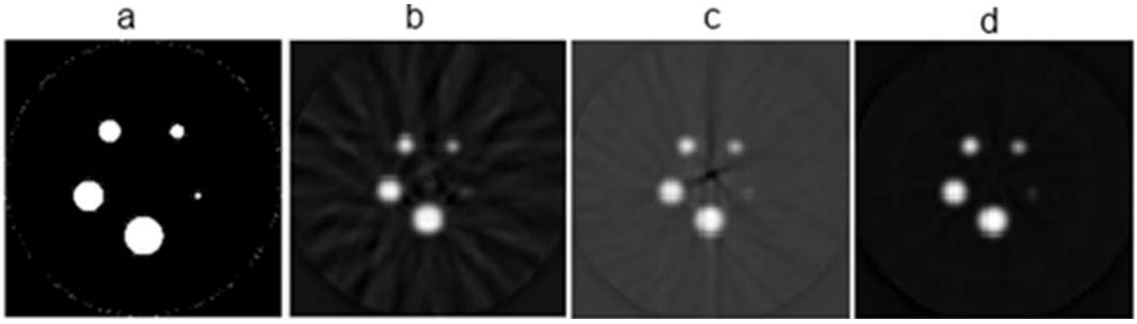

Figure 6.2. *(a) Original NEMA phantom, (b) Gap-filled reconstruction of the phantom without Normalization, (c) Normalized reconstruction, (d) Reconstruction of the phantom after normalizing and gap-filling.*

6.2 AX-PET list-mode data reconstruction

We reconstructed different phantoms scanned with AX-PET demonstrator by using 3DRP. Span9 compression scheme was used. Transradial bicubic interpolation method was applied to estimate the gaps. Dimension of the 3D sinogram and the reconstructed images are shown in the Table 6.1.

Table 6.1. *Dimensions of 3D sinogram and reconstructed image for different sampling.*

Sampling	3D sinogram dimension (radial samples x angular views x slices)	Number of segments	Reconstructed 3D image dimension (X x Y x Z)
1 mm	67x180x1401	17	67x67x153
0.8750 mm	77x180x1737	19	77x77x171
0.4375 mm	153x180x7077	39	153x153x351

Figure 6.3 shows the transaxial and sagittal view of capillaries considering resolution of 1 mm, 0.8750 mm and 0.4375 mm. The resolution of 0.4375 mm suffers streaking artifact due to low statistic list-mode data.

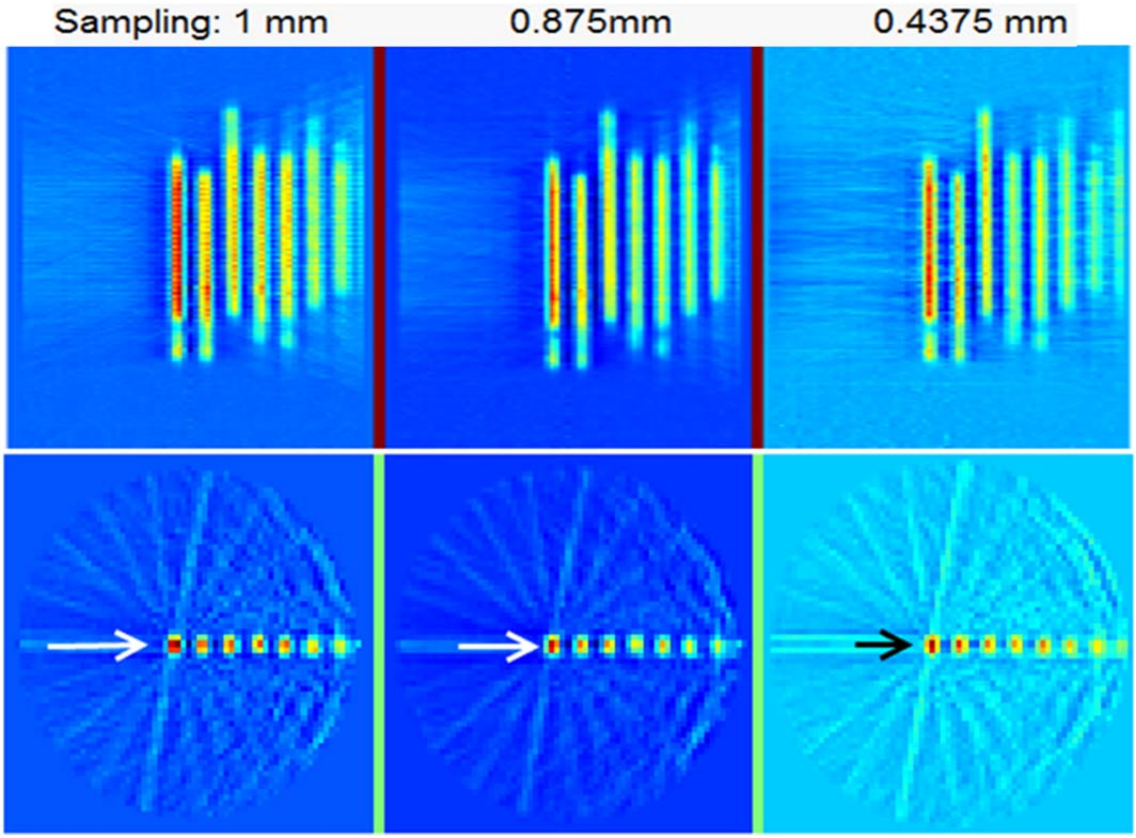

Figure 6.3. *Sagittal (above) and Transaxial (below) view of the reconstructed image of capillary phantom. All of the images are normalized with respect to their own individual counts.*

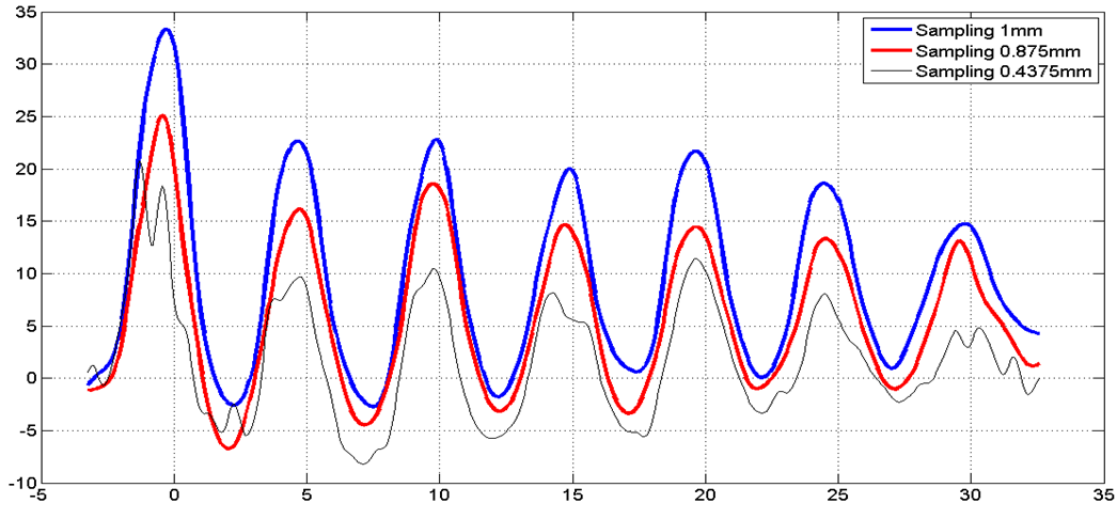

Figure 6.4. *Radial profile of the capillary phantom. The line of profiling is marked in the previous figure with the arrow line.*

Profile of the capillaries shown in Figure 6.4 reveals that the AX-PET concept can avoid the problem of radial elongation. The Full Width Half Maximum (FWHM) measurements of all capillaries are almost same. Figure 6.5 shows the range of FWHM

values for all capillaries and for all sampling. All of the axial slices were considered for measuring FWHM. The vertical line of each FWHM measurement shows the range for all slices. This result is shown in Table 6.2.

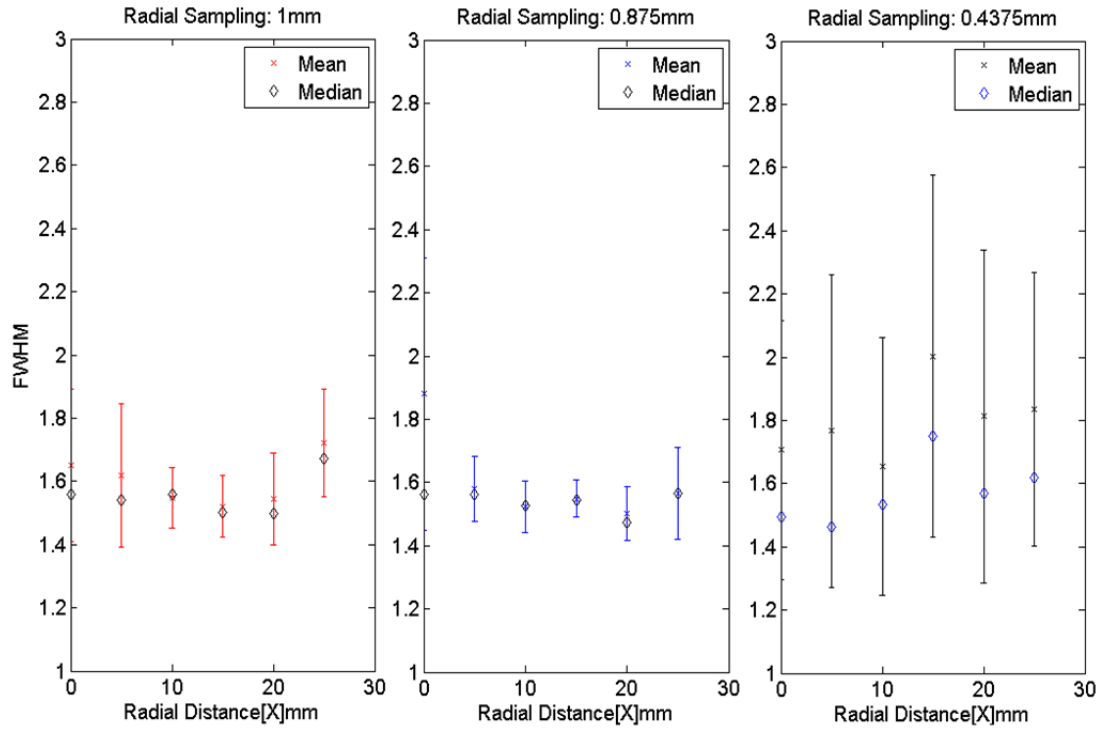

Figure 6.5. *FWHM of the capillaries for the selected sampling rates.*

Table 6.2. *FWHM value for the first six capillaries (counting starts from center of FOV) considering the selected sampling rates.*

Capillary	c1	c2	c3	c4	c5	c6
Sampling 0.4375 mm						
Min	1.3	1.3	1.2	1.4	1.3	1.4
Max	2.2	2.3	2.1	2.6	2.3	2.3
Mean	1.7	1.8	1.7	2.0	1.8	1.8
Median	1.5	1.5	1.5	1.8	1.6	1.6
Sampling 0.875 mm						
Min	1.5	1.5	1.4	1.5	1.4	1.4
Max	2.3	1.7	1.6	1.6	1.6	1.7
Mean	1.9	1.6	1.5	1.5	1.5	1.6
Median	1.6	1.6	1.5	1.5	1.5	1.6
Sampling 1 mm						
Min	1.4	1.4	1.5	1.4	1.4	1.6
Max	1.9	1.8	1.6	1.6	1.7	1.9
Mean	1.7	1.6	1.5	1.5	1.5	1.7
Median	1.6	1.5	1.6	1.5	1.5	1.7

Transaxial view of the reconstructed image of Micro Derenzo phantom A is shown in the Figure 6.6. Figure 6.7 shows the transaxial view of different slices considering sampling of 1 mm.

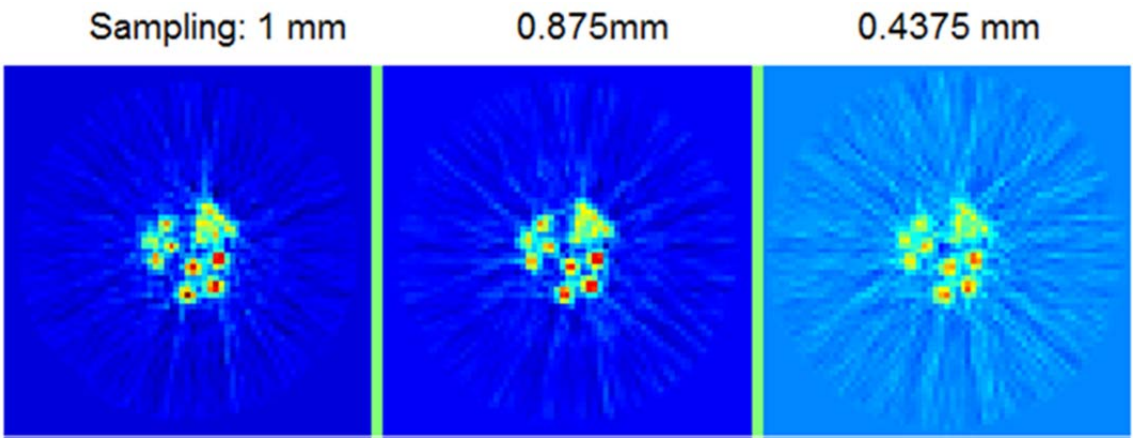

Figure 6.6. *Transaxial view of the reconstructed image of* Micro Derenzo phantom A. *All images are normalized with respect to their own individual counts.*

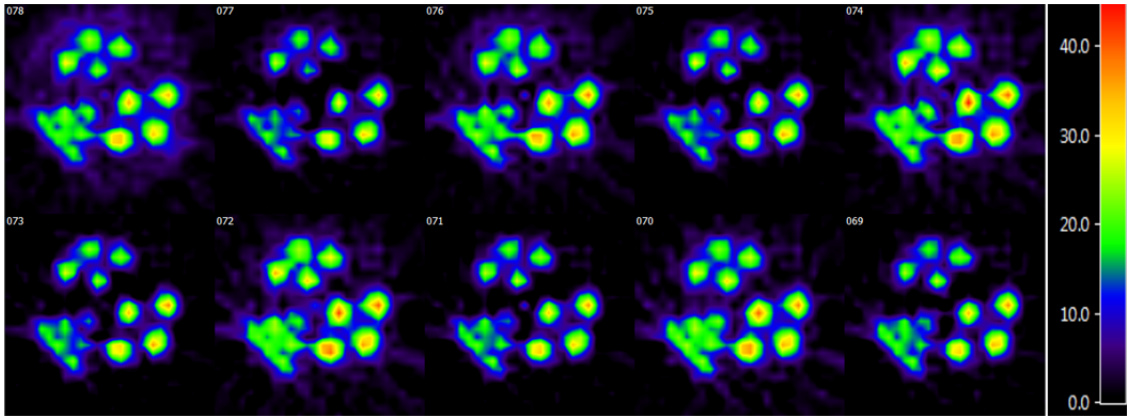

Figure 6.7. *Transaxial view of Micro Derenzo phantom A for the sampling of 1 mm. Consecutive slices show the difference of counts in different axial plane. Scale is not normalized.*

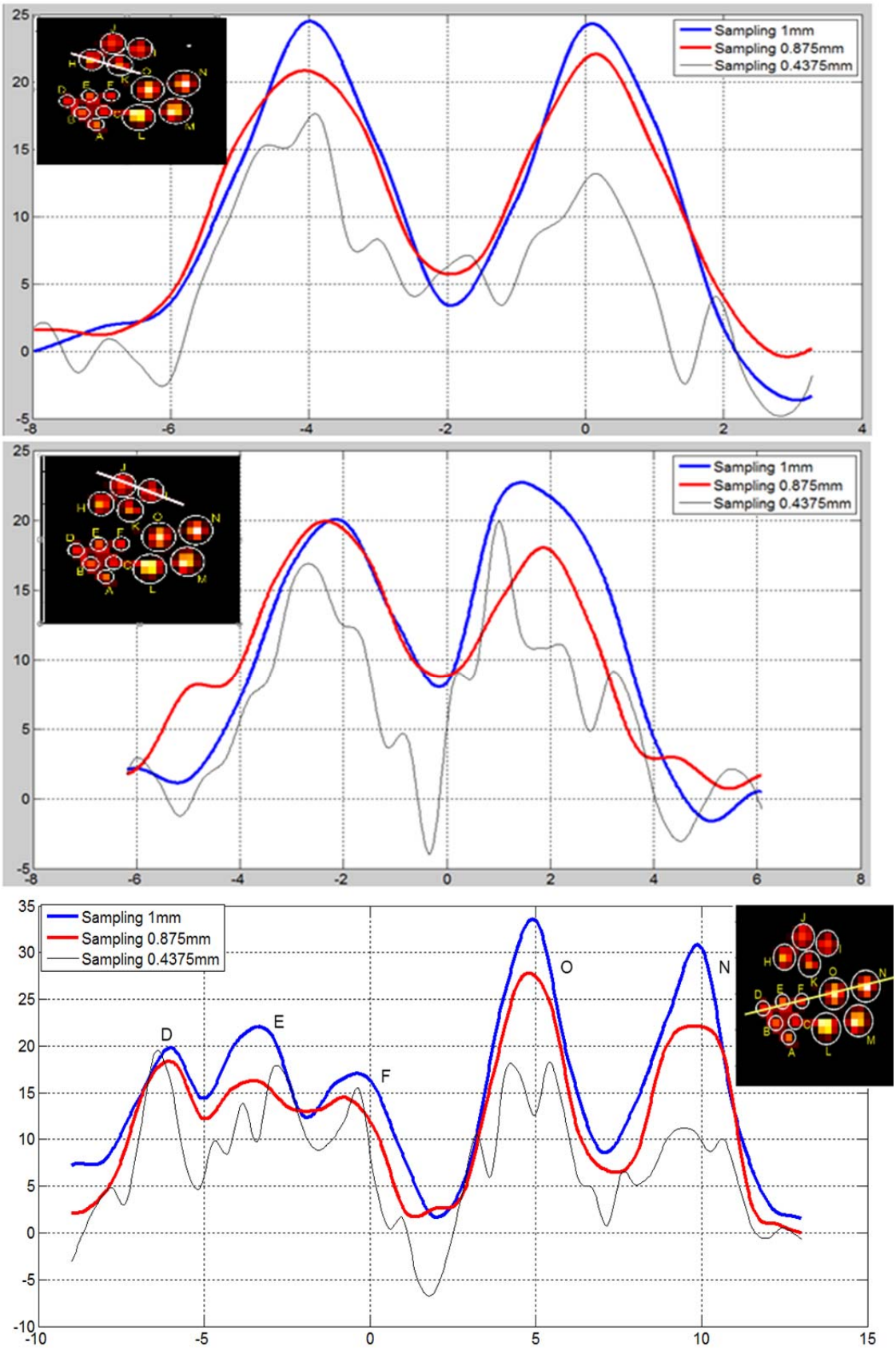

Figure 6.8. *Transaxial view of the Micro Derenzo phantom A (inset) and the profile over the marked region (H, K) in the above figure, (I, J) in the middle figure and (D, E, F, O and N) in the below figure.*

The profile of different insert of the Micro Derenzo phantom A is shown in Figure 6.8. Figure 6.9 shows the FWHM of the different inserts. Table 6.3 shows the FWHM of all inserts.

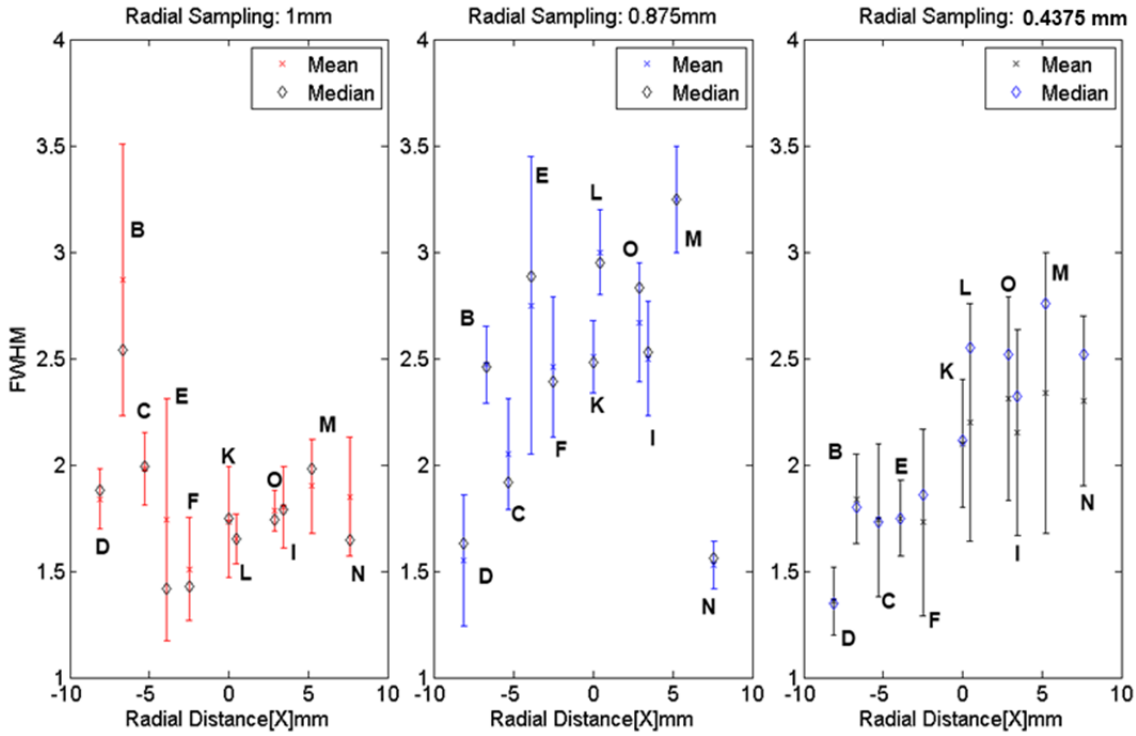

Figure 6.9. *FWHM of different inserts of Micro Derenzo phantom A for selected sampling rates.*

Table 6.3. *FWHM values of the inserts of the Micro Derenzo phantom A for selected sampling rates.*

Insert Diameter	**1.5 mm**						**2.0 mm**				**2.5 mm**			
Insert	A	B	C	D	E	F	H	I	J	K	L	M	N	O
Sampling 0.4375 mm														
Min	1.8	1.6	1.4	1.2	1.6	1.3	1.7	1.7	2.1	1.8	1.6	1.7	1.8	1.8
Max	2.3	2.1	2.1	1.5	1.9	2.8	3.3	2.6	2.8	2.4	2.8	3.0	2.8	2.8
Mean	2.1	1.8	1.7	1.4	1.8	1.7	2.5	2.2	2.5	2.1	2.2	2.3	2.3	2.3
Median	2.0	1.8	1.7	1.4	1.8	1.9	2.1	2.3	2.4	2.1	2.6	2.8	2.5	2.5
Sampling 0.8750 mm														
Min	2.1	2.3	2.1	1.2	1.8	2.1	1.7	2.2	1.6	2.4	2.8	3.0	1.4	2.4
Max	2.4	2.7	3.5	1.9	2.3	2.8	2.3	2.8	2.6	2.7	3.2	3.5	1.6	3.0
Mean	2.3	2.5	2.8	1.6	2.1	2.5	2.0	2.5	2.0	2.5	3.0	3.3	1.5	2.7
Median	2.2	2.5	2.9	1.6	1.9	2.4	1.8	2.5	2.3	2.5	3.0	3.3	1.6	2.8
Sampling 1.0000 mm														
Min	2.0	2.2	1.2	1.7	1.8	1.3	1.4	1.6	1.6	1.5	1.5	1.7	1.6	1.7
Max	3.1	3.5	2.3	2.0	2.1	1.8	2.0	2.0	2.2	2.0	1.8	2.1	2.1	1.9
Mean	2.6	2.9	1.8	1.8	2.0	1.5	1.7	1.8	1.9	1.7	1.7	1.9	1.9	1.8
Median	2.4	2.5	1.4	1.9	2.0	1.4	1.6	1.8	1.9	1.6	1.7	2.0	1.7	1.7

Transaxial, coronal and sagittal views of the reconstructed image of NEMA-IQ-Mouse-Phantom of sequential slices are shown in the Figure 6.10. 1 mm sampling is considered. Figure 6.11 shows the transaxial images for single slice. Selected sampling rates are considered and the images are placed side by side to compare the effect of sampling visually.

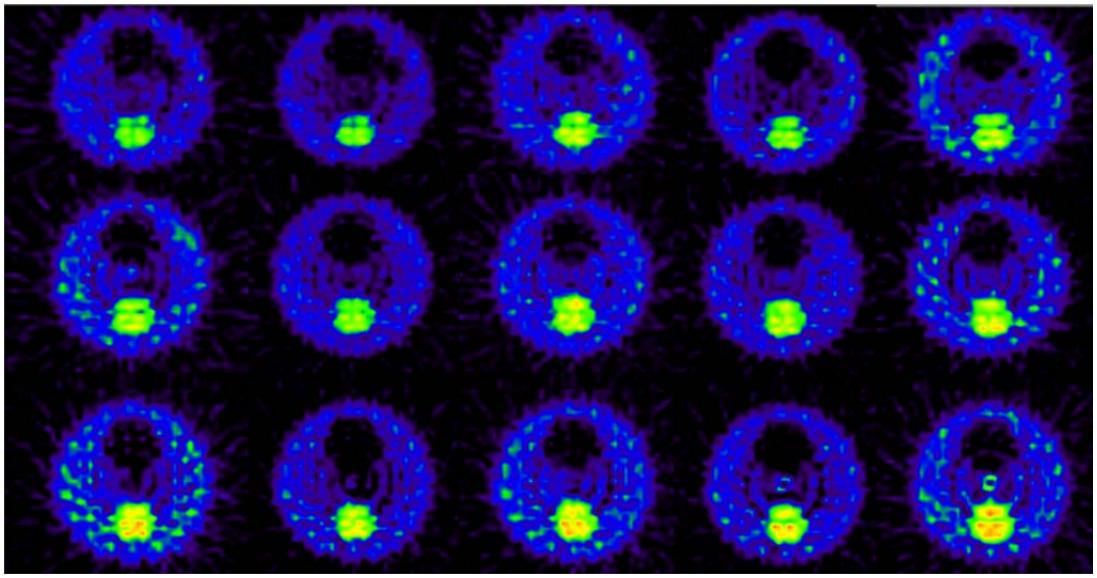

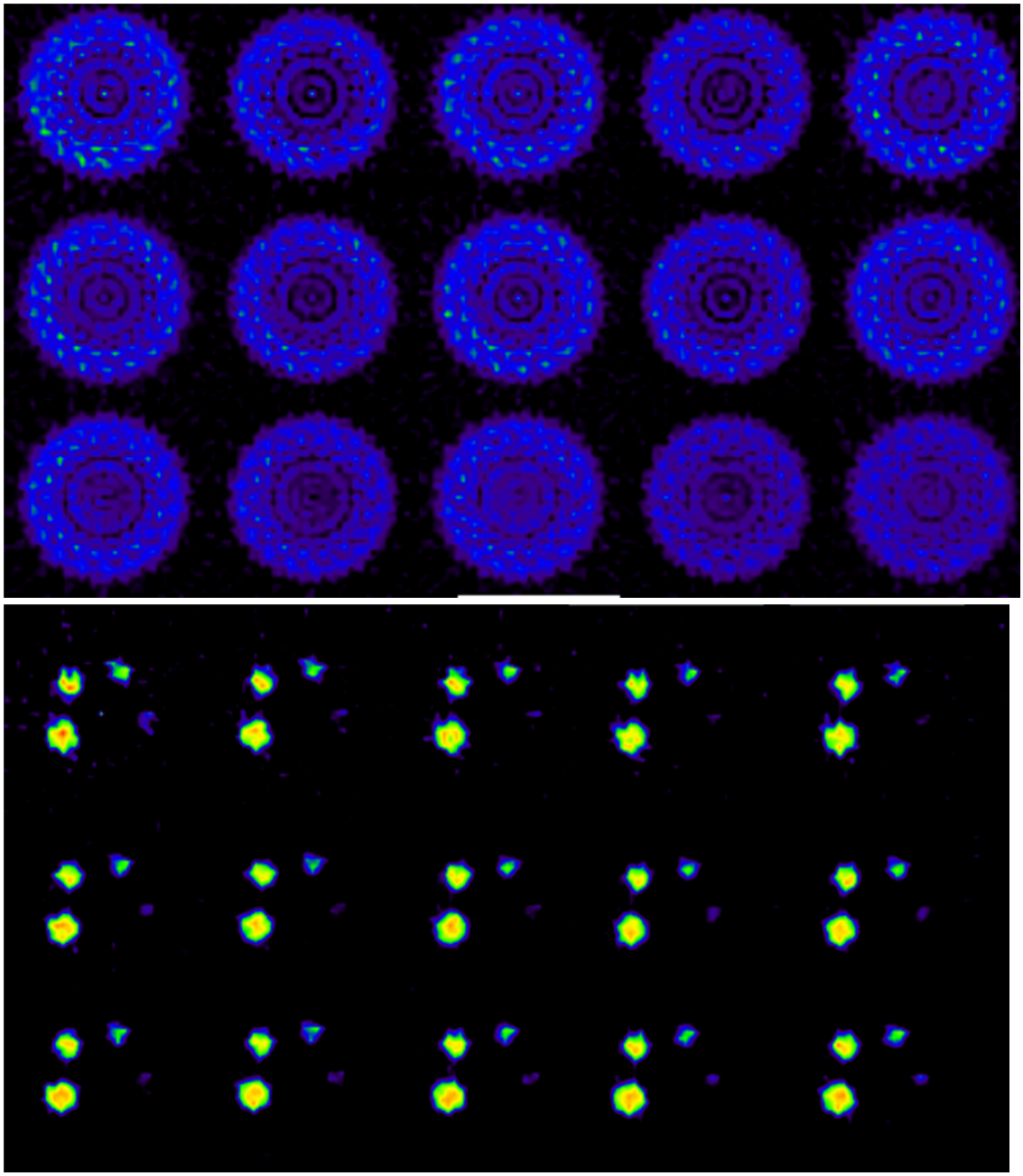

Figure 6.10. *Transaxial view of hot and cold insert (Above), Uniform region (Middle) and 5 inserts (Bottom), of the reconstructed image of several sequential slices of NEMA-IQ-Mouse-Phantom for the sampling of 1 mm.*

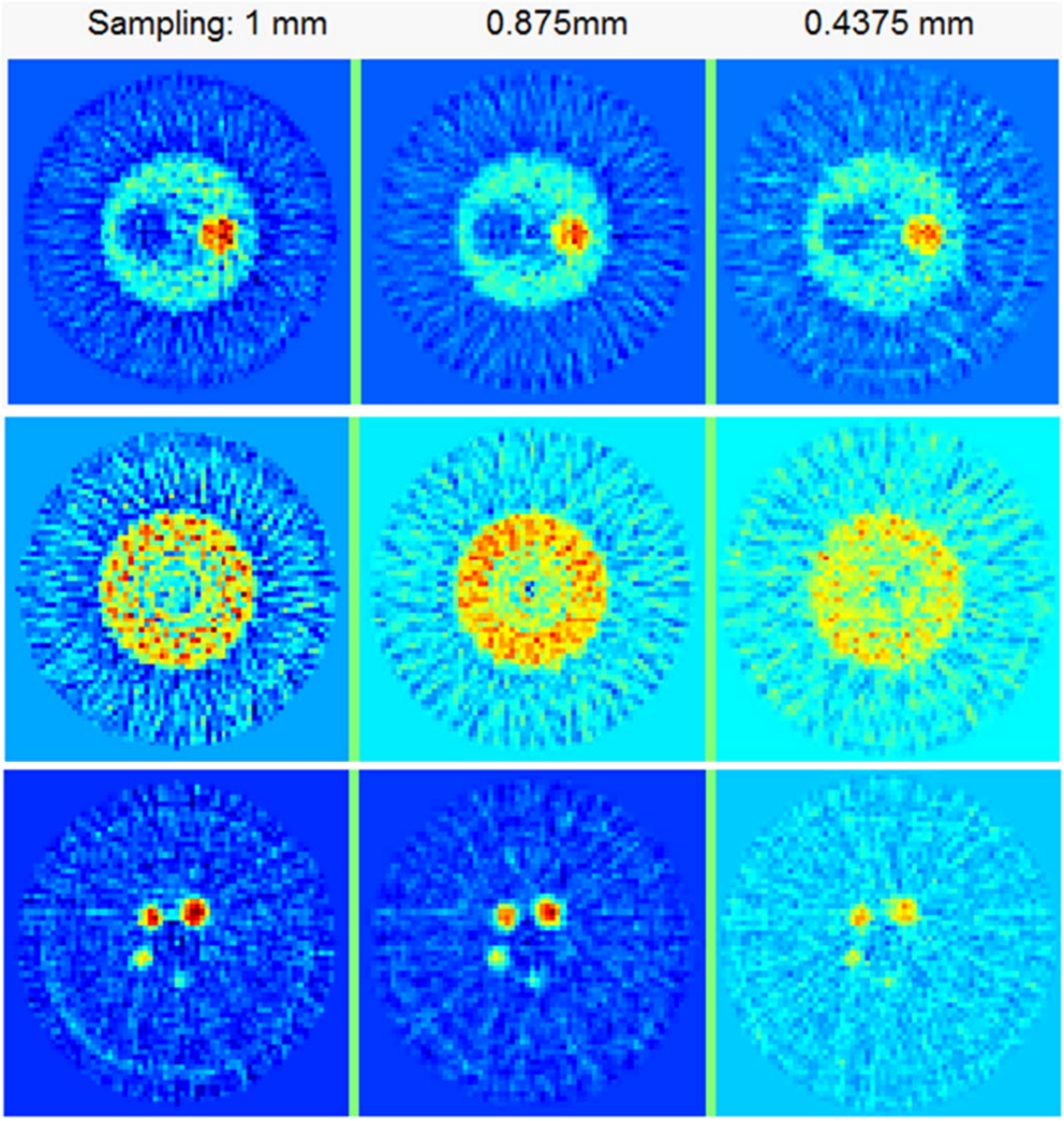

Figure 6.11. *Transaxial view of hot and cold insert (Above), Uniform region (Middle), 5 inserts (Bottom) of the reconstructed image of NEMA-IQ-Mouse-Phantom for selected sampling rates. All of the images are normalized with respect to their own individual counts.*

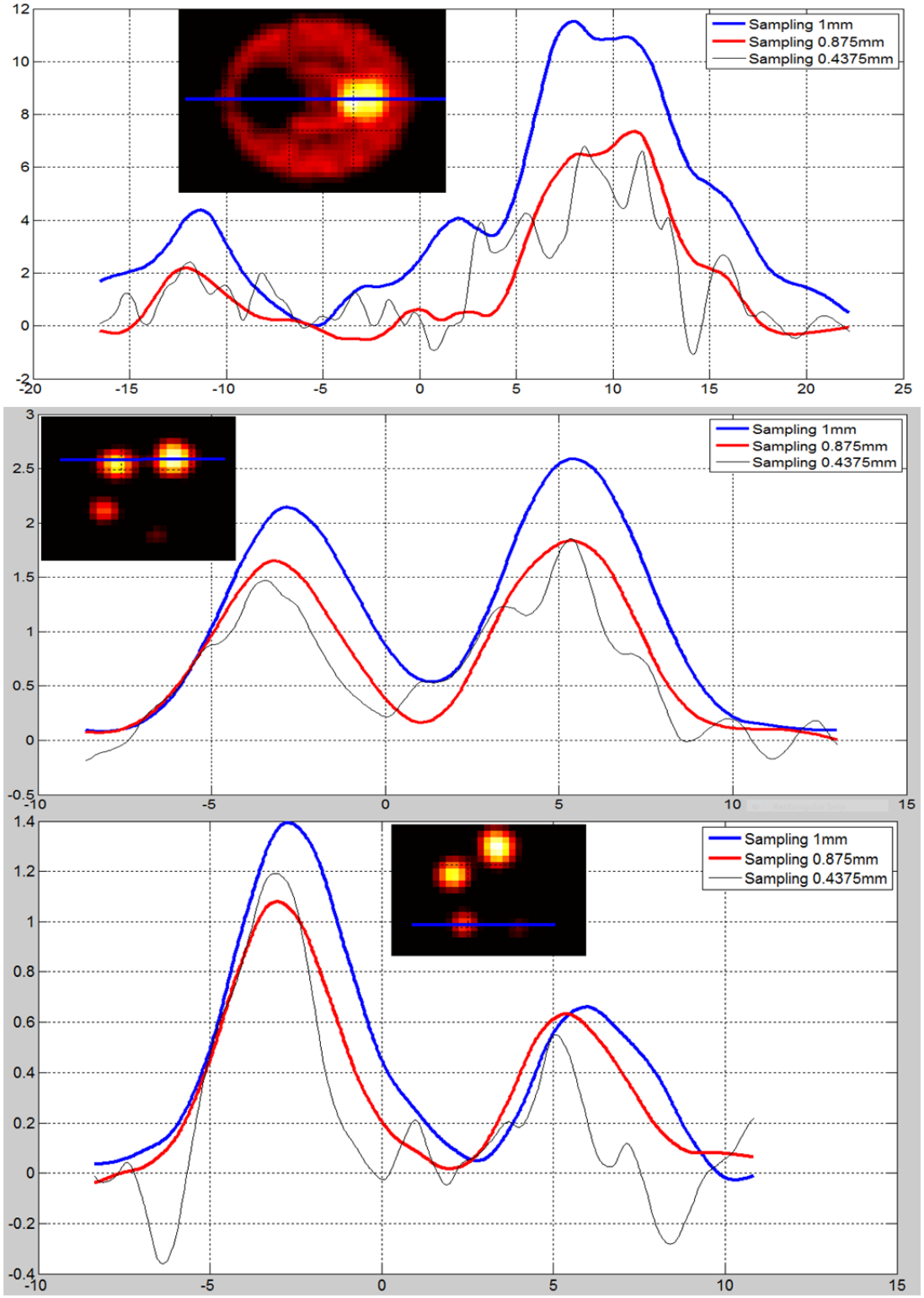

Figure 6.12. *Profile picture of NEMA-IQ-Mouse-Phantom for the selected sampling rates. Above figure shows the profile of hot and cold insert. Middle figure shows the profile of 4 mm and 5 mm inserts and the figure below shows the profile of 2mm and 3 mm inserts.*

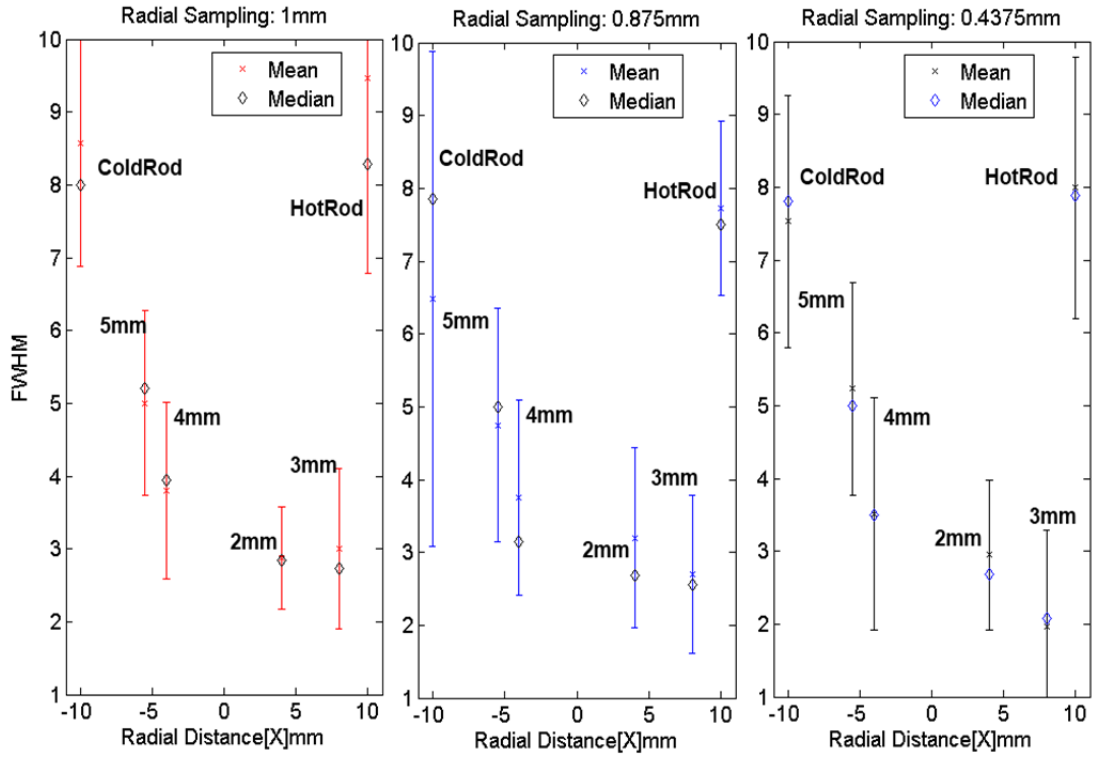

Figure 6.13. *FWHM of different inserts of NEMA-IQ-Mouse-Phantom for the selected sampling rates.*

Table 6.4. *FWHM value of the inserts of the NEMA-IQ Mouse phantom for the selected sampling rates.*

Inserts Diameter	2 mm	3 mm	4 mm	5 mm	Hot Rod (8 mm)	Cold Rod (8 mm)
Sampling 0.4375 mm						
Min	1.6	1.9	1.9	3.8	6.2	5.8
Max	3.2	4.0	5.1	6.7	9.8	9.3
Mean	2.0	3.0	3.5	5.2	8.0	7.5
Median	2.1	2.7	3.5	5.0	8.0	7.8
Sampling 0.8750 mm						
Min	1.6	1.9	2.4	3.2	6.5	3.0
Max	3.8	4.4	5.1	6.3	8.9	9.9
Mean	2.7	3.2	3.8	4.8	7.7	6.5
Median	2.6	2.7	3.1	5.0	7.5	7.9
Sampling 1.0000 mm						
Min	2.0	2.2	2.6	3.7	6.8	6.9
Max	4.2	3.6	5.0	6.3	12.1	10.3
Mean	3.0	2.9	3.8	5.0	9.5	8.6
Median	2.7	2.8	4.0	5.2	8.3	8.0

Figure 6.12 shows the profile of different inserts. Profiles generated from image with 0.4375 mm sampling suffer streaking artifacts due to FBP. Figure 6.13 shows the FWHM of the different inserts. The FWHM for all the sampling rates are consistent with the original dimension of the inserts. Table 6.4 shows the FWHM for all inserts.

Uniformity of the uniform region of NEMA phantom was measured by using CoV (Coefficients of Variation). Figure 6.14 shows the selected region for CoV measurement. All the uniform slices are measured for all the sampling rates. Same figure shows the CoV values.

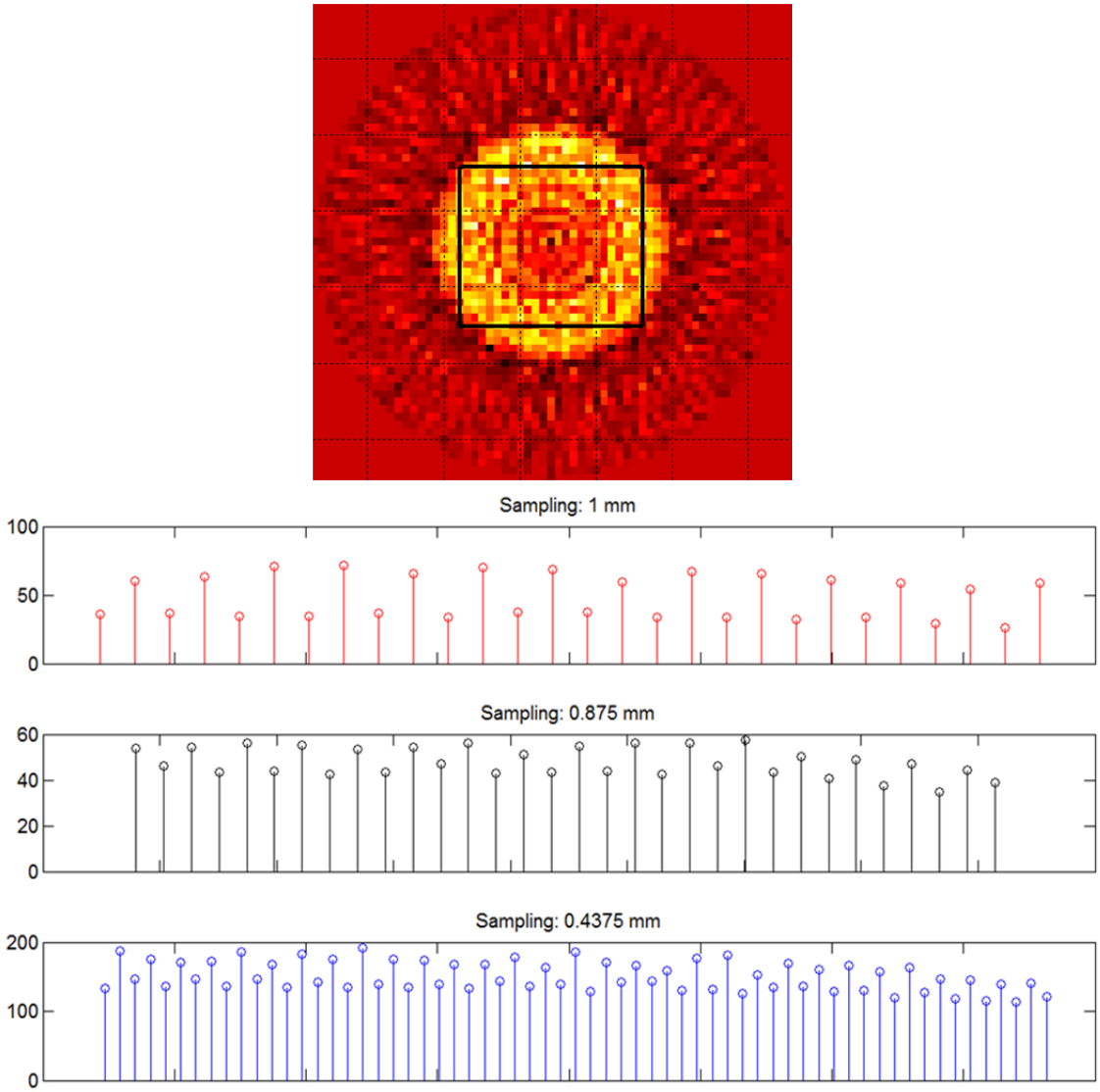

Figure 6.14. *Transaxial image of the uniform region of the NEMA phantom. The selected region for measuring CoV is marked as black rectangle (Above). CoV for selected sampling rates of the selected region (Below). X axis shows the axial direction.*

Transaxial and coronal view of the reconstructed image of uniform cylindrical phantom is shown in the Figure 6.15.

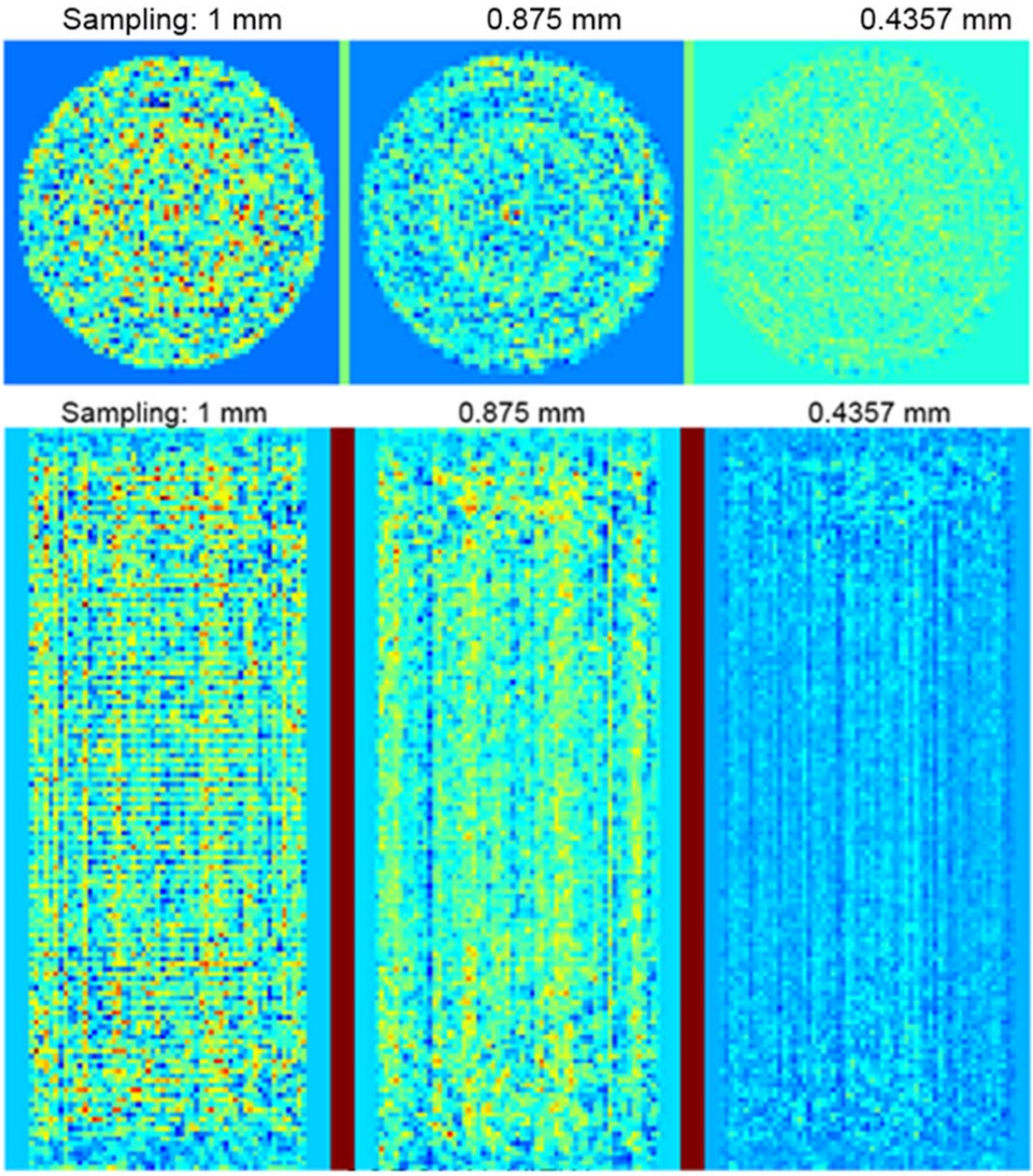

Figure 6.15. *Transaxial (above) and coronal (below) view of the reconstructed image of Uniform Cylindrical Phantom.*

Uniformity of the homogeneous region of uniform cylindrical phantom was measured by using CoV. Figure 6.16 shows the selected region for CoV measurement and the CoV value for the sampling rate of 1 mm, 0.875 mm and 0.4375 mm.

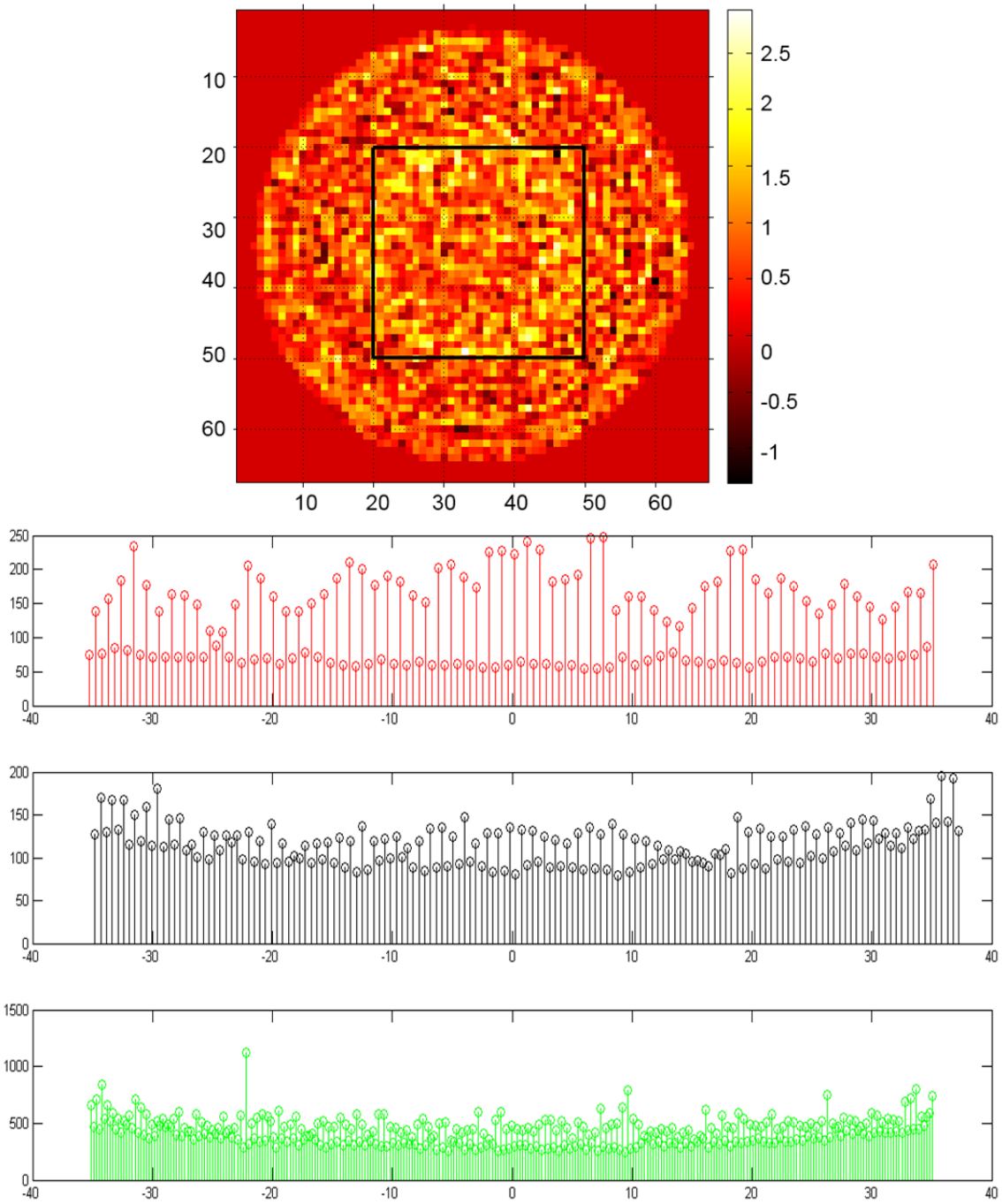

Figure 6.16. *Transaxial image of the uniform region of the cylindrical phantom and the selected region for measuring CoV is marked as black rectangle(Above). CoV for all the sampling of the selected region (Below). X axis shows the axial direction in mm. 0 shows the middle of the axial position.*

Transaxial view of the reconstructed image of Micro Derenzo like phantom is shown in the Figure 6.17. The sampling rate of 1 mm, 0.875 mm and 0.4375 mm were considered.

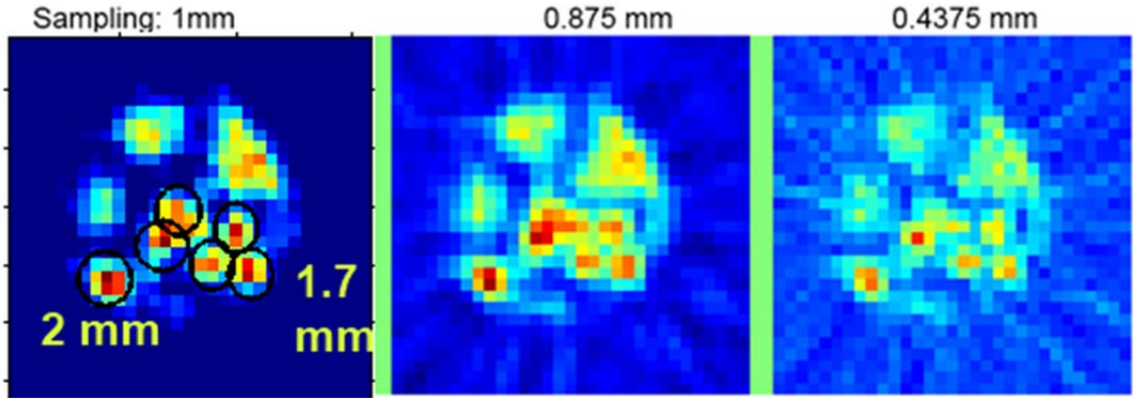

Figure 6.17. *Transaxial view of the reconstructed image of Micro Derenzo phantom B.*

Transaxial view of the reconstructed image of Mini Deluxe Phantom is shown in the Figure 6.18. The sampling rate of 1 mm, 0.875 mm and 0.4375 mm were considered.

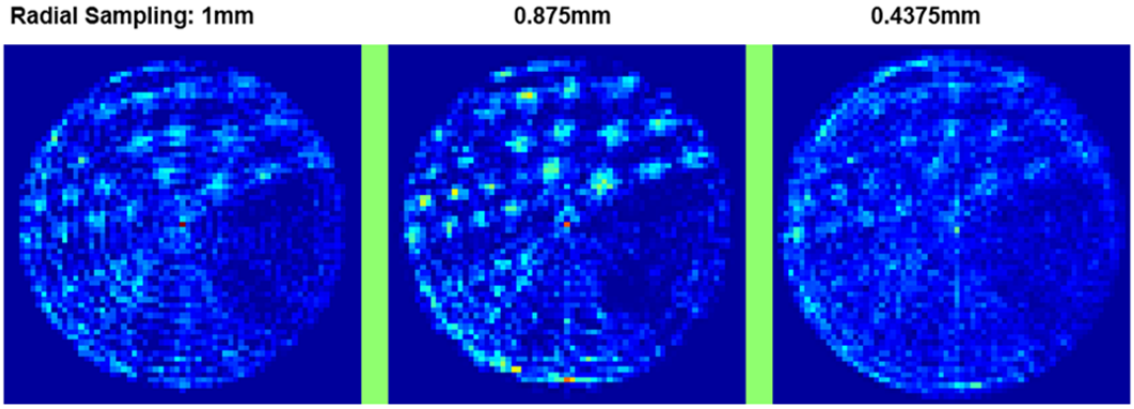

Figure 6.18. *Transaxial view of the reconstructed image of Mini Deluxe Phantom.*

7. Discussion and Conclusion

A comprehensive evaluation of sampling effect on the histogramming and analytical reconstruction of the two module AX-PET demonstrator was performed for the first time and is presented in this thesis. Two types of study were done to test the effect of sampling. FWHM measurement of different phantoms shows that 1 mm sampling is better in resolving small inserts. 1.4 mm inserts of capillary is resolved provided that the pitch of the capillary is more than 2 mm. Coefficient of Variation (CoV) measurement over uniform region of NEMA and uniform phantom reveals noisy artifacts due to low statistics of the list-mode data. Other phantoms of complex structure having different inserts (whose pitch and diameter are not less than 2 mm) can be resolved. It is clear that as we histogram the data with finer radial sampling, the compensation of the inter-crystal gaps becomes harder. Since, the list-mode data has fewer counts, compression scheme of span9 was chosen for histogramming.

Total number of counts in the NEMA phantom A list-mode data is around 20M counts. For different radial sampling for the 3D sinograms, the counts per sinogram bin are shown in Table 7.1.

Table 7.1. *Statistics of data for 3DRP reconstruction.*

Sampling	Sinogram Size	Counts/ Sinogram bin
0.4375 mm	153x180x7077	0.1052
0.8750 mm	77x180x1737	0.8519
1.0000 mm	67x180x1401	1.2138

Observing the reconstructed images, it is clear that 0.875 mm and 1 mm gave good results. Therefore, it should be around 0.85 counts per bin for the 0.4375mm sampling. Hence, the total number of counts should be close to (153x180x7077) x0.85= 165M for 0.4375 mm sampling which is quite hard to achieve.

To give a comparison, for span9 compression of the ECAT HRRT (CTI PET systems, Knoxville, TM, USA) data of [^{11}C]-raclopride study, the net true are around 460M (net true for static sinogram data). It is hard to give comparison because it is impossible to calculate noise-equivalent counts (NECs) for AX-PET data. 460M counts make 2.82 net true counts per bin. That study was framed to have temporal information and the counts/bin is reduced quite a lot especially for the first frames. In general, the number of NECs for a typical raclopride study with HRRT is 200M.

This thesis used MATLAB and STIR. MATLAB implementation for histogramming, normalizing and gap-filling was performed by the author whereas STIR was used without any modification. MATLAB implementations of histogramming can be improved by making it more parameterized so that user can have the option of giving different parameters such as axial compression scheme, dimension of the FOV for the reconstructed image, different radial and axial sampling. Hence, there is a room for improvement in the software. Besides, AX-PET geometry should be implemented in the STIR libraries.

In this study we considered axial (z axis) sampling same as the radial sampling. Since, the counts/sinogram bin are small, we can improve the statistics by taking lower sampling rate in the axial direction. However the option for choosing different sampling rate both for axial and radial direction gives the flexibility of exploring better histogramming and consequently 3D image reconstruction.

The list-mode data are histogrammed with different sampling based on crystal pitch. 1mm sampling shows the best result due to the highest number of counts. Better sampling rate of 0.4375 mm is supposed to give improved resolution. But low statistics data are not sufficient for the reconstruction of that better sampling.

Decreasing the radial sinogram bin below 0.875 mm did not improve the resolution and increased the statistical fluctuations in the image due to the limited number of counts per LOR.

Simulated normalization matrix is the sinogram of the same dimension as the emission sinogram incorporating all the possible LORs. This matrix was made from modified list-mode data based on all combinations of possible LORs in 3D AX-PET scanner. Different phantoms have different counts level and the dimension of FOV also differ. Creating this matrix for one dimension does not match with others. Figure 4.4 shows the sensitivity matrix for the direct plane. This matrix is not symmetrical. Hence, some artifacts are observed in the reconstructed image. This problem of creating sensitivity matrix can be resolved with the high count uniform phantom data.

REFERENCES

[1] M.A. Miller et. al., “Small animal PET imaging,” *Institute of Laboratory Animal Resources Journal,* vol. 49, no. 1, pp.54 - 65, 2008.

[2] P. Beltrame et. al., “Construction and tests of demonstrator modules for a 3-D axial PET system for brain or small animal imaging,” *Nuclear Instruments and Methods in Physics Research Section A: Accelerators, Spectrometers, Detectors and Equipment*, vol. 636, issue. 1, supplement. 21, pp. 226-230, 2011.

[3] P.E. Kinahan and J.G. Rogers, "Analytic 3D image reconstruction using all detected events," *IEEE Transactions on Nuclear Science*, vol. 36, issue. 1, part. 1, pp. 964 – 968, 1989.

[4] M. Rafecas, “The AX-PET Concept: New Developments And Tomographic Imaging,” in press *IEEE Nuclear Science Symposium and Medical Imaging Conference*, 2011.

[5] J. Langner. Development of a Parallel Computing Optimized Head Movement Correction Method in Positron Emission Tomography. Master’s Thesis. University of Applied Sciences Dresden and Research Center Dresden-Rossendorf, Germany, 2003. 153p.

[6] *Positron emission tomography* [accessed on 7.11.2011]. Available at: http://en.wikipedia.org/wiki/File:PET-detectorsystem_2.png

[7] G. B. Saha, “*Basics of PET Imaging Physics, Chemistry, and Regulations”*, 2010, Springer, 241p.

[8] M. Heon et.al. , “A new stationary sampling scheme for multi-layer positron tomographs,” *Nuclear Science Symposium and Medical Imaging Conference*, vol. 3, pp. 1628 – 1634, 1991.

[9] *Supplementary Material Emission Computed Tomography* [accessed on 7.11.2011]. Available at: ric.uthscsa.edu/personalpages/lancaster/DI-II_Chapters/ECT_supplement.ppt

[10] *Image Projections and the Radon Transform* [accessed on 7.11.2011]. Available at: http://www.clear.rice.edu/elec431/projects96/DSP/bpanalysis.html

[11] A. Alessio, P. Kinahan. *PET Image Reconstruction*. [accessed on 7.11.2011]. Available at: http://www.schreisupport.com/Schreisupport/GEN ERAL %20INFORMATION/PET/alessioPETRecon.pdf

[12] D. Platten. *Multi-slice helical CT physics and technology*. EANM 2003 [accessed on 7.11.2011]. available at: http://www.impactscan.org/slides/ eanm2002/ sld014.htm

[13] C. Labbé, H. Zaidi, C. Morel. *Description of the STIR implementation of FBP 3DRP*. Version 0.91. [Accessed on 7.11.2011]. available at: http://stir.source forge.net /documentation/STIR-FBP3DRP.pdf

[14] A. Braem et. al., "AX-PET: A novel PET detector concept with full 3D reconstruction," *Nuclear Instruments and Methods in Physics Research Section A: Accelerators, Spectrometers, Detectors and Associated Equipment,* vol. 610, issue. 1, pp. 192-195, 2009.

[15] P. Beltrame et. al., "The AX-PET demonstrator—Design, construction and characterization," *Nuclear Instruments and Methods in Physics Research Section A: Accelerators, Spectrometers, Detectors and Associated Equipment,* vol. 654, issue. 1, pp. 546-559, 2011.

[16] D. Renker, "New trends on photodetectors," *Nuclear Instruments and Methods in Physics Research Section A: Accelerators, Spectrometers, Detectors and Associated Equipment*, vol. 571, no. 1-2, pp. 1-6, 2007.

[17] B. Gundlich, et. al., "Compensation strategies for PET scanners with unconventional scanner geometry," *IEEE Nuclear Science Symposium Conference Record*, vol.5, pp. 2524 – 2528, 2005.

[18] A. Loukiala et. al., "Gap-filling methods for 3D PlanTIS data," *Physics in Medicine and Biology*, vol. 55, no. 20, pp. 6125-6139, 2010.

[19] The AX-PET homepage. [accessed on 7.11.2011]. available at https://twiki.cern.ch/twiki/bin/view/ AXIAL PET/WebHome

[20] "*Mini and Micro Deluxe Phantom™ & Hot Spot Insert's*" [accessed on 7.11.2011]. available at http://www.spect.com/pub/Mini_and_Micro_Deluxe_ Phantom and_ Hotspot_ Insert.pdf

[21] D. W. Townsend, "*The theory and practice of 3D PET"*, 1998, Springer, 188p.

[22] U.Tuna, S.Peltonen, U. Ruotsalainen, "Interpolation for the gap-filling of the HRRT PET sinograms by using the slices in the direction of the radial samples," IEEE *Nuclear Science Symposium Conference Record*, pp. 3273 – 3279, 2009.

[23] M. M. Akram et. al. , "Analytical Image Reconstruction Strategies for AX-PET data," in press *IEEE Nuclear Science Symposium and Medical Imaging Conference*, 2011.

[24] *"Full Width at Half Maximum (FWHM)*". [accessed on 2.12.2011]. available at http://www.sbig.de/universitaet/glossar-htm/fwhm.htm